Energy & Environmental Science

ROYAL SOCIETY OF CHEMISTRY

PAPER

View Article Online
View Journal | View Issue

Check for updates

Cite this: *Energy Environ. Sci.*, 2025, **18**, 9877

Degradation phenomena in PEMWE revealed by correlative electrochemical and nanostructure analysis

Selina Finger, *[ab] Birk Fritsch, [a] Mingjian Wu, [cd] Leopold Lahn, [ef] Darius Hoffmeister, [ab] Johannes Will, [cd] Olga Kasian, [ef] Erdmann Spiecker, [cd] Simon Thiele, [ab] Anna T.S. Freiberg *[ab] and Andreas Hutzler *[a]

Received 1st July 2025,
Accepted 2nd October 2025

DOI: 10.1039/d5ee03712c

rsc.li/ees

Understanding degradation mechanisms in proton exchange membrane water electrolysis (PEMWE) is critical for advancing the long-term durability of the technology. In this study, we investigate degradation induced by four distinct accelerated stress test protocols through a combination of electrochemical diagnostics and quantitative *ex situ* characterization techniques. We identify multiple interconnected degradation pathways that strongly depend on the operational mode. A key finding is the dissolution of Pt-coating from the anode porous transport layer (PTL), which alters the interface between the PTL and catalyst layer and leads to Pt deposition within the membrane. This process potentially increases the risk of radical formation and chemical membrane degradation. Although Pt coatings on Ti-based PTLs are commonly used to prevent passivation and reduce contact resistance, their role in degradation has been largely overlooked, underscoring the need to assess PTL stability alongside that of the catalyst layers. Additionally, changes in the oxidation state of the Ir-based anode catalyst affect both activity and conductivity. Notably, a higher degree of oxidation is reached when cycling through redox transients compared to operation in steady oxidative regime.

Open Access Article. Published on 10 lokakuuta 2025. Downloaded on 6.2.2026 15.34.04.
This article is licensed under a Creative Commons Attribution 3.0 Unported Licence.

Broader context

One of the most pressing challenges of our time is rapid climate change. Mitigating global warming requires a fast transition from fossil fuels to renewable energy. However, the inherent intermittency of renewable energy sources causes mismatches between supply and demand. Hydrogen offers a promising solution as a large-scale, transportable energy carrier, capable of storing surplus renewable energy – whether spatially or temporally – thereby stabilizing the energy supply. Among the production technologies for green hydrogen, proton exchange membrane water electrolysis (PEMWE) stands out due to its ability to follow rapid load changes, its high power density, and compact system design. Nevertheless, large-scale deployment of PEMWE remains constrained by limited long-term durability, which undermines cost competitiveness against conventional hydrogen production methods. This study uses a correlative approach to quantitatively investigate the performance degradation of PEMWE single cells employing metallic Ir-based anode catalyst layers. By combining electrochemical analysis with advanced electron microscopy techniques, we reveal key degradation phenomena across four distinct accelerated stress test protocols. These insights provide an informed basis for designing operation-specific stress tests and accelerate material development. Moreover, the study concept can serve as blueprint for future investigations on degradation of other electrolyzer technologies.

[a] *Forschungszentrum Jülich GmbH, Helmholtz Institute Erlangen-Nürnberg for Renewable Energy, 91058 Erlangen, Germany. E-mail: s.finger@fz-juelich.de, a.freiberg@fz-juelich.de, a.hutzler@fz-juelich.de*
[b] *Department Chemical and Biological Engineering, Friedrich-Alexander-Universität Erlangen-Nürnberg, 91058 Erlangen, Germany*
[c] *Institute of Micro- and Nanostructure Research (IMN) and Center for Nanoanalysis and Electron Microscopy (CENEM), 91058 Erlangen, Germany*
[d] *Interdisciplinary Center for Nanostructured Films (IZNF), Friedrich-Alexander-Universität Erlangen-Nürnberg, 91058 Erlangen, Germany*
[e] *Helmholtz-Zentrum Berlin GmbH, Helmholtz Institute Erlangen-Nürnberg, Cauerstr. 1, 91058 Erlangen, Germany*
[f] *Department of Materials Science and Engineering, Friedrich-Alexander-Universität Erlangen-Nürnberg, 91058 Erlangen, Germany*

Introduction

In light of climate change, a shift toward a higher market share of renewable energies is inevitable. An energy carrier like hydrogen is needed to bridge demand and supply to effectively use inherently fluctuating renewable energy sources. Additionally, green hydrogen is needed to decarbonize key industries such as steel production.[1] A promising technology to produce green hydrogen is proton exchange membrane water electrolysis (PEMWE) when powered by renewable energies. However,

Open Access Article. Published on 10 lokakuuta 2025. Downloaded on 6.2.2026 15.34.04.
This article is licensed under a Creative Commons Attribution 3.0 Unported Licence.

durability issues still hinder the scale-up toward a gigawatt capacity, amongst other reasons. Long lifetime is especially relevant when employing reduced platinum group metal (PGM) loadings, which is imperative for a scale-up. In particular, good stability is crucial for the cost competitiveness of green hydrogen compared to grey hydrogen.[1]

Current targets for PEMWE technology postulated by the U.S. Department of Energy (DOE) encompass a lifetime of 80 000 h at a degradation rate of 2.3 μV h^{-1} with reduced loadings of 0.5 mg_{PGM} cm^{-2} by 2026.[2] Whereas testing results exceeding 3000 h of operation are rare,[3,4] an increasing number of publications with shorter stability testing periods are available. Currently, degradation rates with established, commercially available materials range from −18 to 400 μV h^{-1}.[3–13] For newly developed catalysts aiming at structural improvements for the challenge of low-loaded catalyst layers (CLs), the degradation rates are higher, ranging between −26 and 2200 μV h^{-1}.[3,4,14–17] The broad range can be explained by varying test conditions (*e.g.*, operation point, operation mode, temperature, pressure, water quality), and varying cell design and components (*e.g.*, material choice, flow fields, transport layer, coating materials, fabrication methods). Thus, comparing results between labs is challenging.

However, it becomes clear that degradation goals have not been reached. To advance prevention or mitigation strategies (regarding design or operation), degradation mechanisms must be understood. Moreover, understanding degradation mechanisms is crucial to develop sensible testing protocols for the development of improved material. Since testing for periods covering the entire lifetime of an electrolyzer is not feasible, the need for the development of accelerated life tests (ALTs) is pressing. Specifically, ALTs must be designed to replicate the degradation mechanisms that occur in real-world operation to guarantee the reliability and lifespan of electrolyzers in industrial applications. To speed up the development of new materials, accelerated stress tests (ASTs) can be designed to study degradation behavior, ultimately contributing to the development of ALTs.

Even though some ASTs have been proposed in the literature, no standardized protocol has been agreed upon in the community. The proposed ASTs focus on current or voltage as stressors, using elevated operation points or dynamic cycling conditions.[5,6,8,12,18–22] In the case of elevated operation, a current density of >2 A cm^{-2} is typically applied.[12,20,22] The cycling periods range from 0.01 s to 10 min, which are considerably shorter than in real operation (*e.g.*, when connected to renewable energy sources) and are deliberately applied to accelerate degradation.[18,19,21] Most publications on ASTs used mainly electrochemical methods to analyze stability.[10,21–24] Some studies included *ex situ* techniques, *e.g.*, electron microscopy techniques, to better understand changes in electrochemical performance.[8,18–20] Voronova *et al.*[12] conducted more extensive *ex situ* investigations in combination with electrochemical analysis. A very extensive *ex situ* end-of-test characterization was performed by Zaccarine *et al.*,[25] however, without providing electrochemical analyses.

In this study, we conducted extensive electrochemical characterization alongside scale-bridging, quantitative *ex situ* analysis to understand the degradation mechanisms emerging in four different stress protocols, designed to simulate the fluctuating electricity price characteristic of renewable energy sources. Our proposed AST protocols try to bridge the gap between often arbitrarily defined sweep-based ASTs and presumed use-cases. The used multi-technique approach combines *in situ* electrochemical methods, such as current–voltage characterization and electrochemical impedance spectroscopy (EIS) in PEMWE single cells, with advanced *ex situ* techniques including X-ray photoelectron spectroscopy (XPS), high-angle annular dark-field scanning transmission electron microscopy (HAADF-STEM), selected area electron diffraction (SAED), STEM energy-dispersive X-ray spectroscopy (STEM-EDXS), and 4D-STEM. Using statistical analysis, we aim to correlate electrochemical performance losses with observed particle precipitation and catalyst oxidation state changes, thereby assessing the consequences of the observed changes. Our insights pave the way to design suitable accelerated stress test protocols for different scenarios.

Study design

The cost-competitiveness of green hydrogen produced *via* PEMWE compared to grey hydrogen highly depends on electricity prices.[1,26] Thus, PEMWE becomes economically viable when low-cost electricity is available. This typically occurs in 6-hour intervals, based on stock electricity prices, when energy generation exceeds the load (Fig. S1a).[27] To simulate these operating conditions and assess the resulting degradation effects, we designed four stress protocols to study the induced degradation. A square-wave protocol, compared to a triangle-wave protocol, more closely mimics real operation conditions and induces more severe degradation,[18] making it the preferred choice. A current density of 2 A cm^{-2} is chosen for full load operation of the PEMWE single cells.

Given the focus of this study on elucidating degradation mechanisms for AST development, the intervals of the electricity-price profile (Fig. S1a) are shortened to 6 min[19,28] and the periods of shut down are simulated by applying a potential of 27 mV (AST-0, see Fig. 1a and Fig. S1b). The lower potential is motivated by the cell potential reached after longer open-circuit voltage (OCV) periods as explained in the SI. For the ease of readability, we call this hold at lower potential OCV though it is strictly speaking not the natural open-circuit voltage reached during the fast AST protocols. AST-0 is compared to three variations: AST-freq, where the cycling frequency is increased 6-fold,[19,28] AST-amp, where a shutdown is avoided[5,22] (cycling between 1 A cm^{-2} and 2 A cm^{-2}) and AST-CC, where cycling is avoided entirely (constant-current operation). The protocols are illustrated in Fig. S1 and summarized in Fig. 1a.

For each AST protocol, one cell with pristine components (gaskets, PTLs, GDLs, and CCMs employing metallic iridium as anode catalyst) is used. After conditioning of the cells, each testing protocol is applied four times for 24 h with intermittent

 This journal is © The Royal Society of Chemistry 2025

Open Access Article. Published on 10 lokakuuta 2025. Downloaded on 6.2.2026 15.34.04.
This article is licensed under a Creative Commons Attribution 3.0 Unported Licence.

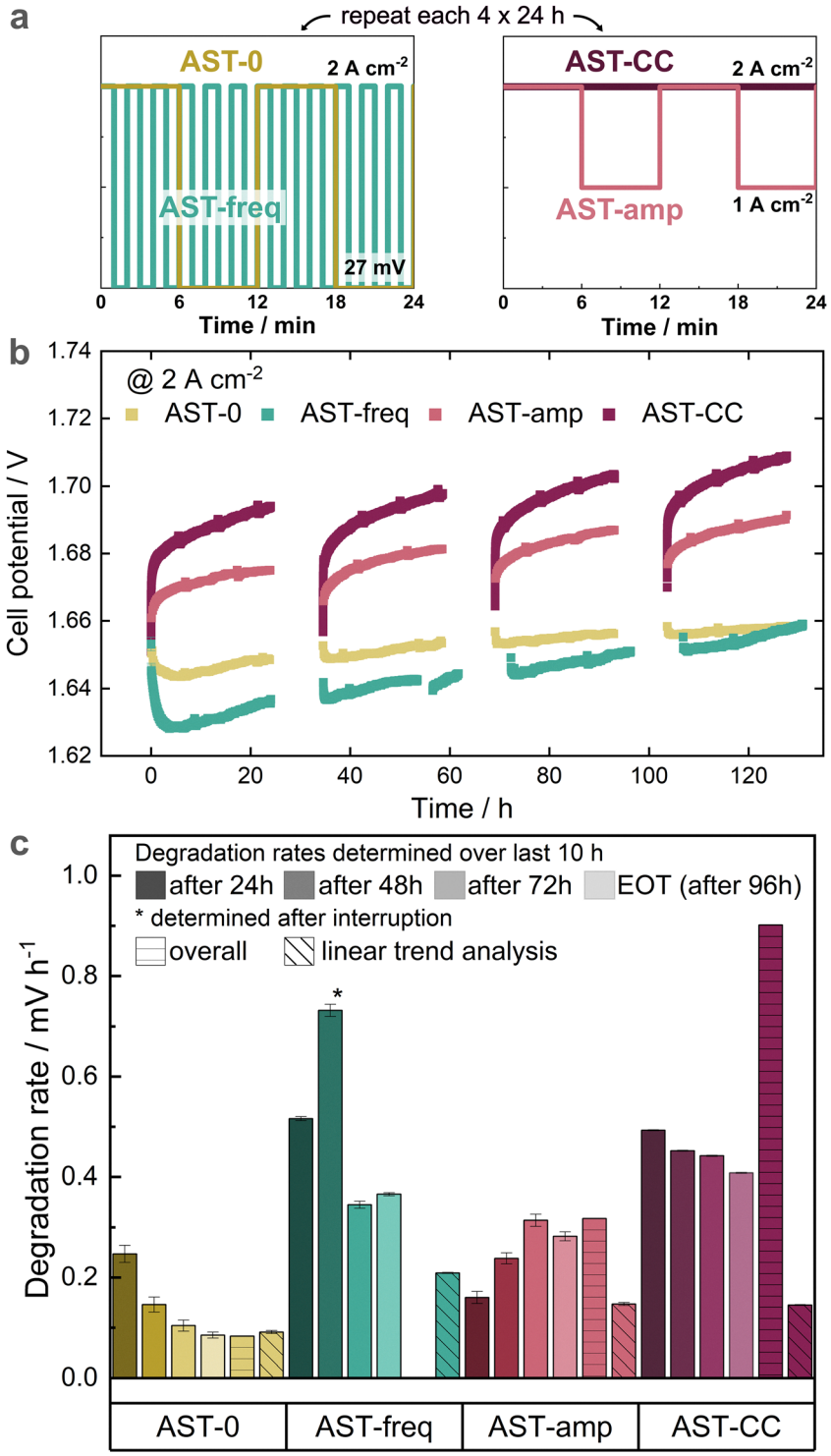

Fig. 1 (a) Four different ASTs used in this study. Each was repeated four times for 24 h with intermittent characterization. (b) Potential evolution throughout the different stress tests. (c) Degradation rates calculated with the potential at beginning (BOT) and end of test (EOT) (called 'overall'), from linear trend analysis and within each 24-h step. Within each 24-h period, the last 10 h were used for a linear fit, and the slope ± standard deviation is shown. Each experiment was performed with pristine CCMs with Ir black-based anode (1.65 ± 0.09 mg_{Ir} cm^{-2}), Nafion NR212 membrane (~51 μm) and Pt/C-based cathode (0.15 ± 0.06 mg_{Pt} cm^{-2}). The anode features a Pt-coated Ti-fiber transport layer (2GDL10-0.25) and the cathode a carbon-based transport layer (H24C5). All cells were operated at 80 °C with 100 ml min^{-1} water supply to the anode and a dry cathode.

electrochemical characterization every 24 h. Additionally, beginning-of-test (BOT) and end-of-test (EOT) characterization was conducted. For BOT conditions, three individual tests are performed to ensure that the stress tests start out from a comparable condition.

Open Access Article. Published on 10 lokakuuta 2025. Downloaded on 6.2.2026 15.34.04.
This article is licensed under a Creative Commons Attribution 3.0 Unported Licence.

For *ex situ* characterization, various techniques were applied to the CCMs after cell disassembly and to 100 nm-thick ultramicrotomy slices of the CCMs from the four different test protocols. As a reference, a CCM which was in the PEMWE cell only for conditioning (termed 'conditioned') was additionally characterized.

Electrochemical performance evolution

As depicted in Fig. 1a, four ASTs were conducted, each for a total time of 96 h. Fig. 1b shows the potential evolution over time at 2 A cm^{-2} from the different stress tests. Notably, the potential evolution can be divided into two groups based on observations from Fig. 1b. AST-amp and AST-CC exhibit immediate performance losses, whereas AST-0 and AST-freq initially improve at the beginning of each cycling period, followed by a performance decay. A similar behavior was reported by Alia *et al.*[5] with a commercial IrO_x anode catalyst, and by Weiß *et al.*[22] using commercial IrO_2/TiO_2 as the anode material. The difference between these two groups is that the redox transient of the anode catalyst is avoided for AST-amp and -CC by keeping the potential above $\sim$1.4 V,[29] as analyzed later. Overall, AST-CC evolves to the highest potential at EOT.

For comparison, Fig. 1c shows the degradation rates obtained for the different ASTs derived from Fig. 1b. Two approaches were used to determine the global degradation rates during stress testing. In the first approach, the difference between the starting and end potential during the current holds is normalized by the total time to calculate the overall rate (termed 'overall'). The second approach only accounts for irreversible losses, where the end potential within each 24-h period is used for a linear trend analysis (see explanation in SI and Fig. S2). These two approaches reveal a different trend. For the overall degradation rate, AST-CC shows the highest rate, whereas the degradation rate for AST-freq is essentially zero due to a strong initial performance improvement. In contrast, AST-freq has the highest degradation rate from linear trend analysis because the performance decrease after the initial improvements is the highest. Within each 24-h period (as determined in the last 10 h of the ASTs), the highest degradation rates are observed for AST-freq and AST-CC.

When comparing the irreversible losses within the two groups (avoiding *vs.* cycling through redox transitions), it becomes clear that higher degradation is observed for higher cycling frequency (AST-0 *vs.* AST-freq). AST-amp and AST-CC show comparable performance degradation even though AST-CC operates for a prolonged time at higher current densities.

Analysis of degradation

To understand the origin of the described losses, correlative electrochemical and *ex situ* analyses have been performed.

Electrochemical analysis

First, data gathered at BOT, after each 24-h period, and at EOT from polarization curve measurements and electrochemical impedance spectroscopy (EIS) is compared in Fig. 2. For all graphs in Fig. 2, an average BOT condition with standard deviation from separate tests is displayed in green, showing that the BOT performance of the CCMs undergoing the different stress tests (except AST-CC) is comparable. AST-CC shows an increased high-frequency resistance (HFR) at BOT, which generally causes a higher cell potential. This is assigned to a variation in PTL thickness leading to a reduced interfacial contact due to compression, which was revealed after testing. To make sure that the observations are comparable, HFR-free cell potentials and CVs are shown (Fig. 2b and Fig. 3a–c) revealing that the difference only originates from the HFR. Hence, AST-CC is included since general trends can be observed.

The cell potential change at 2 A cm^{-2} from the polarization curves is displayed in Fig. 2a. The trends match the observations from the potential evolution within the 24-h periods of stress testing (compare Fig. 1b). Interestingly, no improvement of the HFR (Fig. 2c) for AST-freq and AST-0 is visible after the first 24 h as seen in the evolution of cell potential (Fig. 2a). The initial improvement is probably a kinetic phenomenon connected to the redox transient of the anode catalyst, since it is visible from the HFR-free cell potential (Fig. 2b).

Kinetic overpotentials. The activity of the catalyst for the oxygen evolution reaction (OER) highly depends on the oxidation state of the catalyst and the amount of available active sites. After HFR-correction, the polarization curves contain contribution from kinetics, residual ohmic electrode resistance and mass transport. At 2 A cm^{-2}, mass transport contributions are assumed to be low. Hence, in Fig. 2b, a low HFR-free potential reflects an electrode with high activity, either purely due to fast kinetics of the catalyst or high catalyst utilization caused by low ohmic losses throughout the catalyst layer. The latter will be discussed in the next sub-chapter. The HFR-free potentials of AST-0 and -freq decrease initially and gradually increase afterward (Fig. 2b). At EOT, AST-0 and -freq still possess the lowest HFR-free potential because AST-amp and -CC show a gradual increase from the beginning.

In terms of oxidation state, Ir metal provides superior activity over Ir oxide.[30,31] Hydrous or substoichiometric Ir oxide has shown even higher OER activity.[32,33] The observed initial improvement in activity could be due to a dissolution-induced roughness increase of the surface and, thus, more available active area.[34] Another explanation could be the formation of hydrous or substoichiometric Ir oxide at the catalyst surface.[22,29,32] While hydrous Ir oxide should be present to a certain extent in all tests, it is preferably formed from substoichiometric Ir^{3+} or Ir^{4+}. Substoichiometric Ir oxide is likely present to a higher extent for AST-freq and AST-0 because of the operation through redox transients as also discussed based on the *ex situ* data later.[32]

A decrease in activity could be connected to the formation of anhydrous Ir oxide. However, an influence from a change in available active sites due to a restructuring of the catalyst

 This journal is © The Royal Society of Chemistry 2025

Open Access Article. Published on 10 lokakuuta 2025. Downloaded on 6.2.2026 15.34.04.
This article is licensed under a Creative Commons Attribution 3.0 Unported Licence.

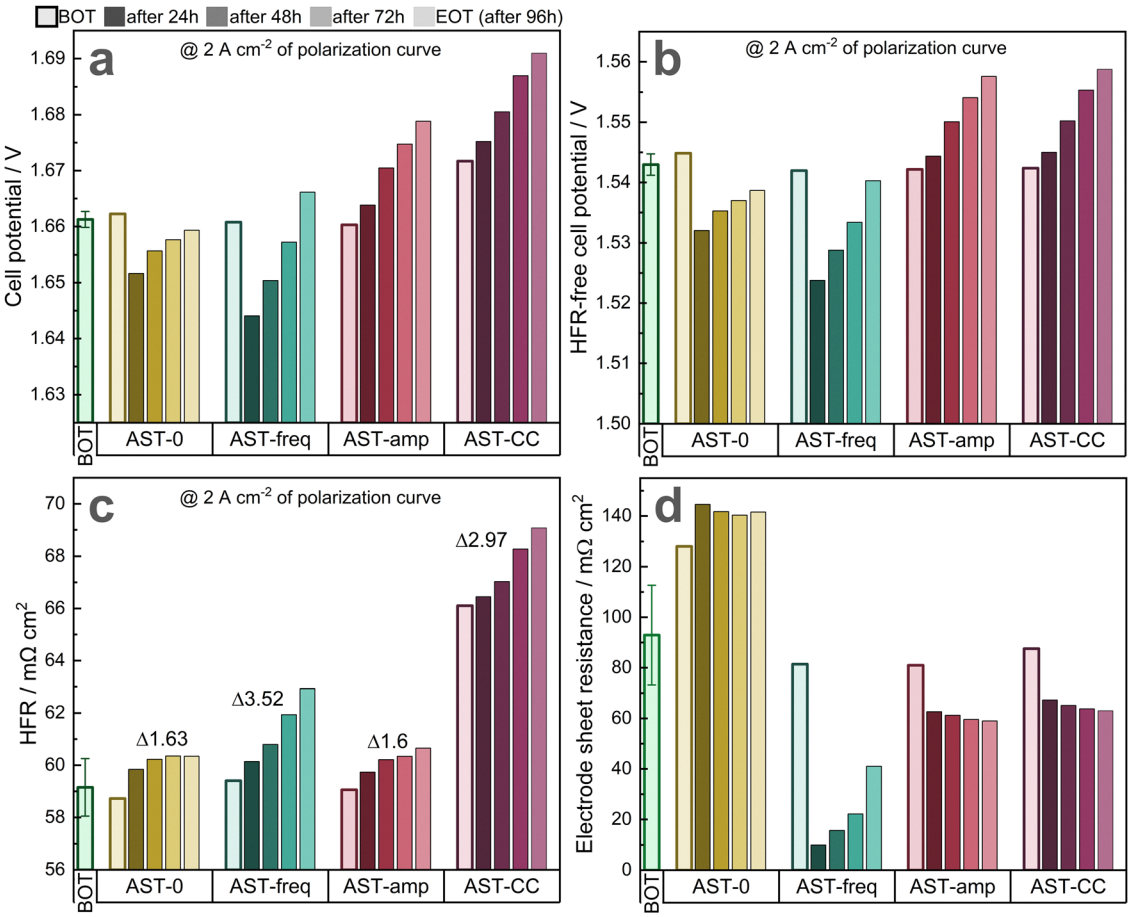

Fig. 2 Electrochemical characterization of the CCMs at BOT, after each 24-h period and EOT of the stress testing. Within each plot a mean BOT condition ± standard deviation (green bars) is included as reference from three independent cells with the same specifications. One of these CCMs is also used for *ex situ* characterization termed 'conditioned' sample. (a) Cell potential evolution and (b) HFR-free cell potential evolution from polarization curves at 2 A cm^{-2}. (c) HFR evolution from the fitting of galvanostatic EIS data recorded along with the polarization curves. The complete polarization curve data is shown in Fig. S3. (d) Electrode sheet resistance (ESR) measured *via* potentiostatic EIS at 1.25 V cell potential (*i.e.*, in non-faradaic conditions).

surface during the oxidation state changes cannot be excluded. The Tafel slopes in Fig. S4a give insights into the activity of the active sites available and confirm a similar trend to the HFR-free potential. Fig. S4a shows almost no change in Tafel slope for AST-amp but a gradual decrease in activity over prolonged stress testing for AST-CC. For AST-0 and -freq an initial improvement in activity is followed by a decay. Similarly, Kuhnert *et al.*[20] and Alia *et al.*[5] observed an improved initial performance originating from kinetic improvements.

The trends observed for the HFR-free cell potential (Fig. 2b) can be connected to changes in the cyclic voltammograms (CVs) in Fig. 3a–c and Fig. S4b–f. At BOT (Fig. 3a), all tests show characteristic hydrogen underpotential deposition (H-UPD) features at 0.1–0.5 V typical for metallic Ir.[35] Another peak is visible at around 0.75 V assigned to Pt oxidation and reduction of the Pt-coating on the PTL.[36] Interestingly, the Pt features disappear for AST-0 and -freq over the testing period. We hypothesize that the Pt is reduced largely during shutdown periods so that oxidation does not occur fast enough during the CVs.

In all cases, the distinct H-UPD features decrease over prolonged stress testing (see also Fig. S4), indicating a change in the surface oxidation state. A change in surface observed from CVs is also visible for Weiß *et al.*,[22] where changes appear more drastic for cycling through redox potentials. As depicted in Fig. 3c, the final state is similar for AST-0 and -freq, and for AST-amp and -CC, respectively, which is in line with the cell potential evolution (Fig. 1b) and the change in HFR-free cell potential (Fig. 2b). However, the end state is reached at a different pace. While for AST-freq, the changes in CV features are only minor after the first 24 h (the shape is already very similar to EOT), AST-0 shows gradual changes over time. The CV for AST-0 after 24 h hints toward both metallic (partly sustained H-UPD) and (hydrous) Ir oxide (reversible oxide redox feature between 0.5 V and 1.2 V), which is also observed after cycling with IrO_2-based catalyst.[22,29] Surprisingly, this shape is not visible after 72 h of stress testing. One hypothesis is that the formed hydrous Ir oxide may be anchored differently when starting out with IrO_2 compared to the Ir metal used in our case, as the oxide growth mechanism depends on the surface on which it is growing.[37] Besides growth mechanisms, the underlying surface can influence the properties of the grown oxide layer.[37] Thus, it could be less stable over prolonged stress

Open Access Article. Published on 10 lokakuuta 2025. Downloaded on 6.2.2026 15.34.04.
This article is licensed under a Creative Commons Attribution 3.0 Unported Licence.

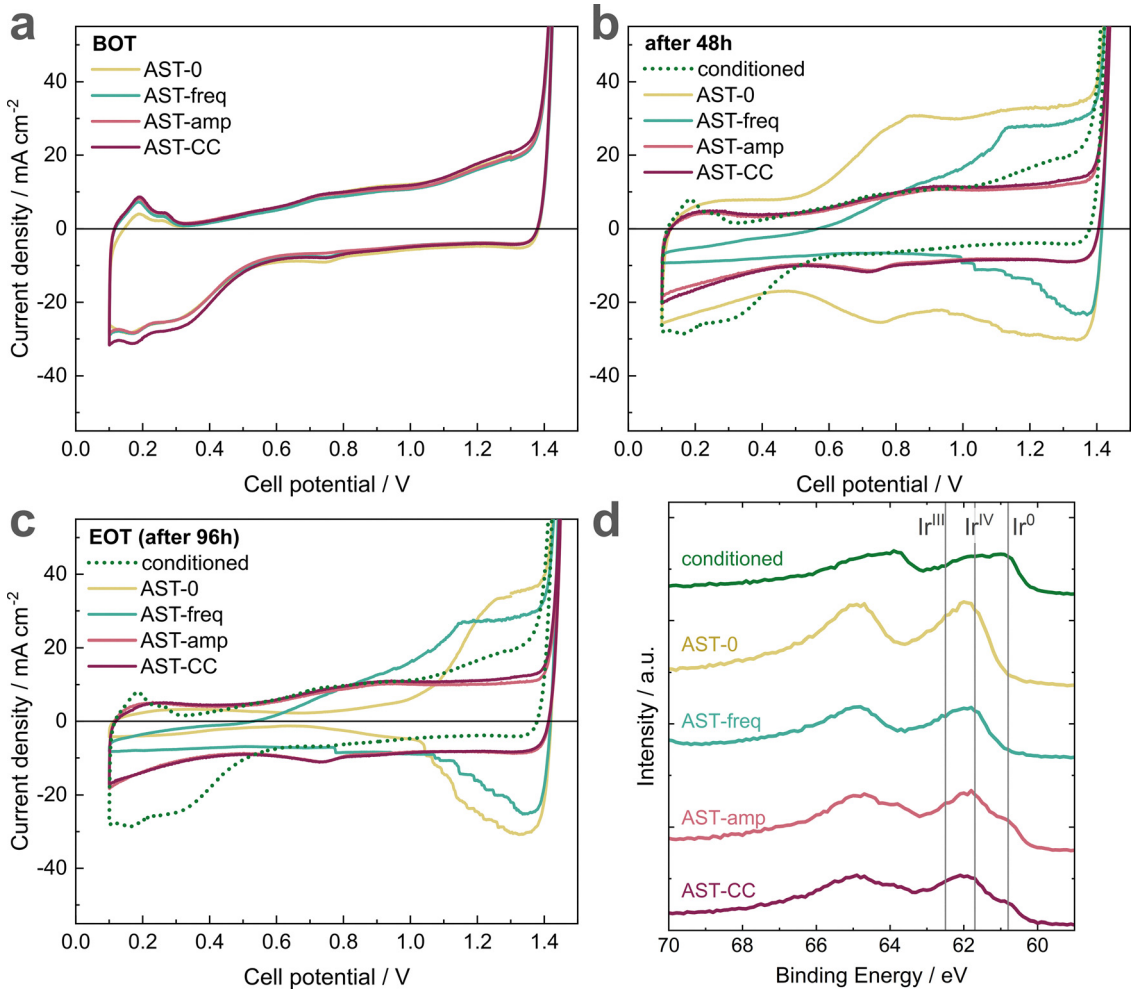

Fig. 3 (a)–(c) Cyclic voltammograms (CVs) of all stress tests at BOT, after 48 h of stress testing, and at EOT. CVs are recorded at a scan rate of 50 mV s^{-1} and 80 °C. H_2 was produced electrochemically on the cathode prior to the recording. (d) XPS measurement of EOT CCMs on the anode catalyst layer. The reference binding energies for the Ir oxidation states were chosen according to literature.[40–42] More extensive XPS data and survey scans can be found in Fig. S6 and S7b, c, respectively. All stress tests are depicted along with a CCM for reference that only experienced conditioning ('conditioned').

testing when grown on Ir metal. The shape of the CVs, recorded at EOT after AST-0 and -freq resemble the shape of CVs of hydrous Ir oxide shown in literature.[34,38] Especially the small capacity at low potentials <0.6 V hints toward hydrous Ir oxide.[29]

The CVs of AST-amp and -CC evolve features of Ir oxide as observed in CVs of rutile IrO_2.[39] However, a small feature toward the H-UPD region suggests a contribution from metallic Ir, especially for the first 48 h of cycling. At EOT, the metallic features have almost vanished. However, XPS (Fig. 3d) reveals that at EOT, AST-amp and -CC still show contributions from metallic Ir (Ir^0). The difference can be attributed to the changes induced when the cell is shut down and disassembled or a difference in probing depth between XPS and CV. For AST-0 and -freq, the XPS results exhibit only oxidic features in line with the CVs at EOT. Note that with XPS, the EOT states of the anode catalyst layer (CL) surfaces facing the PTL were measured.

Catalyst oxidation can occur during all stress tests, specifically during the non-idle phases of the testing period. A catalyst reduction only occurs in case of a reductive potential regime (roughly <1.4 V for Ir) or in the presence of H_2 as a reductive agent when the potential is not controlled.[29] Hydrogen crosses over from the cathode to the anode in all cases. A reductive regime is present for AST-0 and -freq for a total of 48 h (50% of the testing time) when the potential is dragged down to 27 mV. However, as evident from Fig. 1c and 3a–c, AST-freq underwent more drastic/fast changes than AST-0. The amount of switching differs between the two tests (six times higher cycling frequency for AST-freq). Thus, the transient condition seems to especially promote changes, which can be partially attributed to alterations in the oxidation state, as also observed previously.[5,22] A change in oxidation state is expected to cause changes in activity as discussed before.

It was shown that dissolution occurs during the formation and reduction of an oxide layer and is notably concurrent with the build-up of hydrous Ir oxide and with occurring OER.[34,35] The dissolution during hydrous oxide formation can be explained by a prevalent model from Pickup and Birss:[43] first,

 This journal is © The Royal Society of Chemistry 2025

Open Access Article. Published on 10 lokakuuta 2025. Downloaded on 6.2.2026 15.34.04.
This article is licensed under a Creative Commons Attribution 3.0 Unported Licence.

a thin and compact anhydrous oxide layer is formed on the Ir metal surface when increasing the potential (>1.4 V). Secondly, a porous hydrous Ir oxide layer builds on top of the anhydrous layer. The oxide growth rate depends on the current density.[35] In the case of an oxidative regime, the growth of a hydrous Ir oxide layer is self-limiting because it prevents further oxidation towards the core.[43] When cycling to reductive potentials, however, the compact, anhydrous layer dissolves (partially), enabling the continuing formation of hydrous oxide when cycling again to higher potentials.[43] Notably, oxide formed at higher potential may not be reduced entirely during cycling so that there is a net growth of the oxide layer.[35] It was further shown that dissolution occurs to a larger extent in the reductive regime than for oxidation.[44] Hence, we expect a higher dissolution and net growth of an oxide layer for AST-0 and -freq. For AST-amp and -CC, the growth of a self-limited oxide layer is expected. The dissolution is discussed based on nanostructure analysis below.

Ohmic overpotentials. From EIS measurements, the HFR in Fig. 2c was derived as a measure of ohmic resistance in the cell. Further data from EIS measurements can be found in Fig. S5. It is evident from Fig. 2c, that AST-freq shows the highest HFR increase over the testing period. An increase in HFR could originate from several sources: an increase in contact resistance between PTL and CL originating from a structural change of the interface, a build-up of less conductive Pt oxide (compared to metallic Pt[45]) on the PTL, or a change in electrical conductivity of the CL due to its structure and the oxidation state of the catalyst. A possible loss of proton-conducting groups in the membrane due to chemical degradation or blockage by metal ions could increase the HFR further. Conversely, thinning of the membrane due to chemical degradation would decrease the HFR but could be overshadowed. The different influences are discussed in the following.

To exclude thinning of the membrane, the CCM cross-sections were measured with scanning electron microscopy (SEM) after testing. As can be seen from Fig. S8, no thinning is observed and the membrane thickness after testing equals to 54.0 ± 4.0 μm. A structural change of the PTL|CL interface is possible because dissolution and redeposition of Pt and Ir are detected as discussed further below (Fig. 5 and Fig. S15, S17). Additionally, it is noteworthy that on the CL side facing the PTL, Pt is detected for AST-0, -freq, and -amp *via* XPS. In contrast, it was not detected for AST-CC and the conditioned sample (Fig. S6b).

To separate the contribution of CL resistance from the ohmic resistance expressed with HFR, the electrode sheet resistance (ESR, see Fig. 2d) is measured *via* EIS in non-faradaic conditions.[46] The ESR can be influenced by a change in catalyst electrical conductivity and the electrical and protonic conductivity of the CL. Note that the electrical resistance of the CL is partially included in HFR and ESR, depending on its magnitude.[47]

Fig. 2d shows that the ESR changes within the first 24 h and is stable afterward for AST-0, -amp, and -CC. Since the change in the first 24 h is not reflected in the HFR, it may originate from protonic resistance changes caused by a restructuring of the ionomer film during oxidation state changes of the catalyst surface (as observed from CVs). Conversely, the ESR of AST-freq increases after an initial decrease. This trend can be caused by a complex interplay between the protonic and electrical resistance of the CL. A change in protonic resistance due to chemical ionomer degradation is not expected because the fluorine content measured *via* STEM-EDXS (Fig. S9a) shows similar values for all tests. However, a restructuring of the ionomer within the CL is conceivable. The electrical resistance of the CL is influenced by the conductivity of the bulk catalyst material and the formed percolation network between crystallites.

The electrical conductivity of the catalyst itself is influenced by its oxidation state. Ir suboxide exhibits significantly lower conductivity than crystalline IrO_2 powder (factor 200–600).[48,49] Metallic Ir powder shows a conductivity in the range of IrO_2 or even higher (see Fig. S10). Additionally, changes in the oxidation state may alter the electrical percolation network within the CL as conductivity also depends on the connectivity and geometry of crystallites and clusters. Depending on the different oxidation states of Ir, the catalyst volume changes because of density differences (ρ_{Ir} = 22.65 g cm^{-3} *vs.* ρ_{IrO_2} = 11.66 g cm^{-3} *vs.* ρ_{hydr,IrO_x} = 1–2 g cm^{-3} [50]). A transition from metallic Ir to IrO_2 doubles the volume, while conversion to hydrous Ir oxide increases it approximately eleven-fold. An indication of this volume change is seen in HAADF-STEM measurements (Fig. S12a–e) and quantified by Ir-area coverage analysis from HAADF-STEM data (Fig. S9b). It reveals a slight increase of Ir coverage by 6 ± 3% and 8 ± 2% for AST-0 and AST-freq, respectively.

In case of an increased volume, an improvement in electrical percolation is possible.[51] However, this is again connected with a change in the inherent conductivity of the catalyst particles, which follows the opposite trend ($V_{hydr,IrO_x} > V_{IrO_2} > V_{Ir}$ and $\sigma_{Ir} \geq \sigma_{IrO_2} > \sigma_{hydr,IrO_x}$) and influences from the percolation network. Their respective contribution, however, remains unclear from the available data. At lower loading, the effects described could become more severe since there is less material to buffer a restructuring or losses. It can still be concluded that the most considerable changes in HFR and ESR are observed for AST-freq, but their origin needs further investigation.

Analysis of catalyst-coated membrane (CCM) ultramicrotomy slices

Ex situ analyses were conducted on EOT CCM samples from all AST protocols, along with a reference CCM sample subjected only to initial conditioning (called 'conditioned') to investigate the origins of the observed performance losses.

Structural analysis. The structural overview in Fig. S11 shows the anode CL consisting of sheet-like structures (Fig. S11h) and larger Ir clusters of a few hundred nanometers evenly distributed throughout the electrode (Fig. S11a–e). The fluorine content is evenly distributed (Fig. S11g and j), hinting toward uniform ionomer dispersion. The large-scale structure before and after stress testing remains similar, and no significant cracks or disruption of the electrode is visible (see also Fig. S8

Open Access Article. Published on 10 lokakuuta 2025. Downloaded on 6.2.2026 15.34.04.
This article is licensed under a Creative Commons Attribution 3.0 Unported Licence.

and Fig. S13a–e). Interestingly, the magnified images in Fig. S12a–e reveal that while AST-amp and -CC exhibit a similar structure to the conditioned sample, the sheet-like structures after AST-0 and -freq appear changed toward a cotton ball-like structure. *Via* HAADF-STEM image analysis, a slight change in the areal coverage of the Ir phase for AST-0 and AST-freq (Fig. S9b) was detected. As mentioned earlier, this could influence the electrical percolation pathway within the CL and/or the ionomer wetting of the Ir particles.

The structural change is assigned to an oxidation state change as determined from phase mapping with nano-beam 4D-STEM (Fig. 4f–j and Fig. S14b–f). In the conditioned sample, AST-amp and -CC, the portion of the rutile phase is small (less than 1.4%), whereas the portion of the rutile phase in AST-0 and -freq are both more than 30%. A similar picture becomes evident from distortion corrected SAED analyses[52] in Fig. 4l (corresponding bright-field TEM images of selected areas and SAED patterns in Fig. 4k and Fig. S12). It is evident that the conditioned sample shows mostly face-centered cubic (fcc) reflections of metallic Ir. AST-amp and -CC exhibit a mixed phase of rutile IrO_2 and metallic fcc Ir, which is shifted more towards rutile IrO_2 for AST-0 and -freq. 4D-STEM and SAED mainly quantify crystalline phases. However, the sloping background observed in Fig. S14a indicates the presence of amorphous phases. While some of the amorphous signal can be attributed to the ionomer in the CL and to carbon from the sample holder, the steeper slope for AST-amp and -CC and then even steeper for AST-0 and -freq indicates a significant increase in amorphous iridium oxide. Amorphous iridium oxide phases are also evident from CVs and XPS (Fig. 3) but are only a qualitative measure. SAED shows the highest amount of amorphous phases for the two samples cycled through redox potentials (AST-0 and AST-freq).

Via 4D-STEM we additionally obtain spatially resolved information about crystal structure and orientation because diffraction patterns in each pixel alongside real space dark field

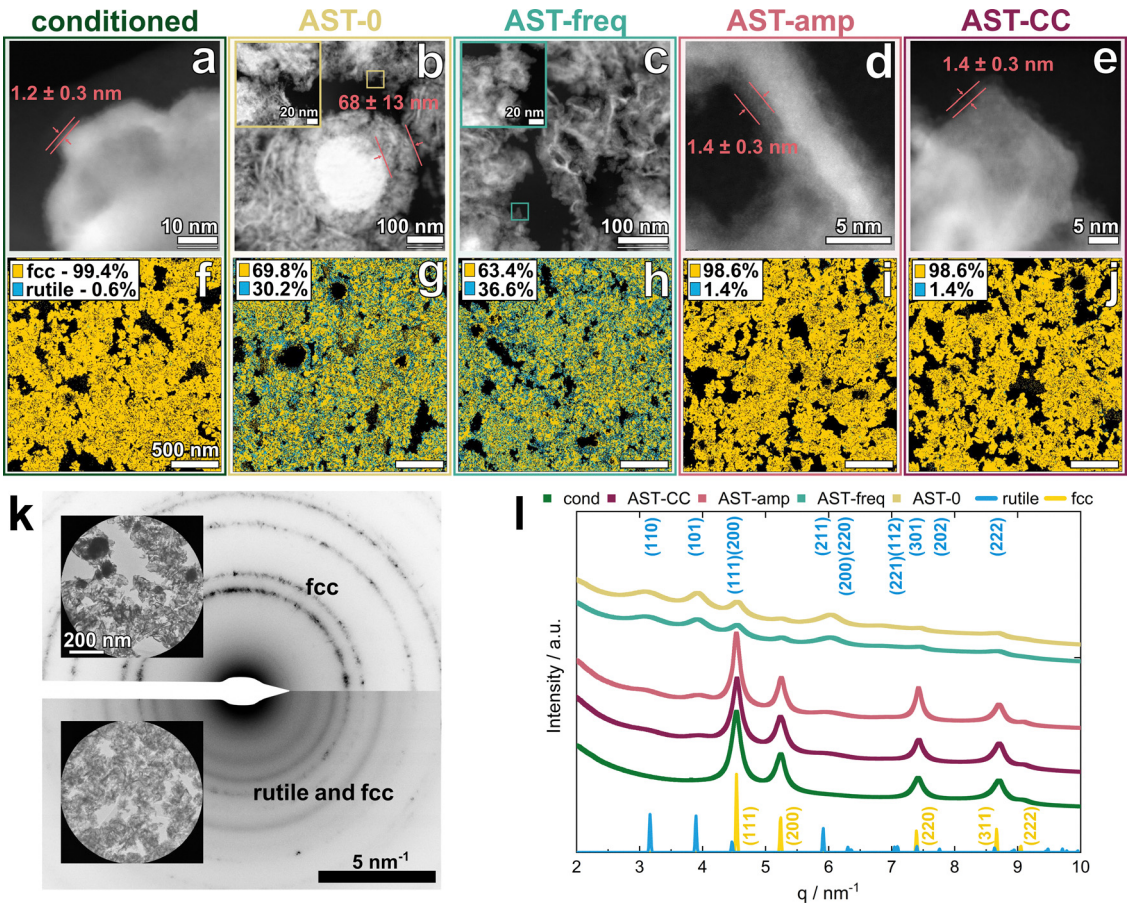

Fig. 4 *Ex situ* characterization of the anode catalyst layer at EOT after all stress tests and after conditioning as reference. The measurements are performed on ~100 nm slices cut with an ultramicrotome from embedded CCMs: (a)–(e) HAADF-STEM images of Ir particles within the CL. Thickness measurement of oxide thickness was performed using ImageJ. The mean value ± standard deviation from seven points is shown. (f)–(j) Phase map from 4D-STEM showing the distribution of fcc metallic and oxidic Ir and their atomic fractions. Corresponding Bragg vector maps are shown in Fig. S14b–f. (k) Exemplary SAED pattern of CLs and corresponding selected areas as insets. Top: SAED from conditioned sample showing characteristic pattern of fcc Ir. Bottom: SAED from AST-0 showing characteristic pattern of mixed rutile IrO_2 and fcc. SAED from all stress tests can be found in Fig. S12. (l) Intensity *vs.* reciprocal lattice vector q of distortion-corrected SAED patterns.[52] q is the reciprocal scattering vector where $1/q$ corresponds to lattice plane distances in real space. Reference spectra for Ir and IrO_2 are retrieved from inorganic crystal structure database (ICSD). Note that the plots are intensity normalized and shifted along the y-axis to improve readability. See Fig. S14a for raw data.

 This journal is © The Royal Society of Chemistry 2025

Open Access Article. Published on 10 lokakuuta 2025. Downloaded on 6.2.2026 15.34.04.
This article is licensed under a Creative Commons Attribution 3.0 Unported Licence.

images are recorded. This allows us to identify at which positions a metallic fcc phase, an oxidic rutile phase, or a superposition of both phases is present. Fig. 4f–j shows that the oxide covers the metallic core in the form of a surface layer.

A thin layer of 1–2 nm on the Ir particles for the conditioned, AST-amp, and AST-CC sample can be visualized *via* HAADF-STEM, as shown in Fig. 4a, d and e. AST-0 shows a 40-fold increased thickness of this layer, and for AST-freq many of the Ir clusters changed their structure all the way to the core (Fig. 4b and c). Lattice fringes with distances matching 110 and 101 planes of rutile IrO_2 have been identified in this layer (Fig. 4a, d and e), suggesting that this layer is oxidic in line with the 4D-STEM analysis. Additionally, the peaks in the SAED patterns corresponding to rutile IrO_2 are remarkably broadened compared to metallic fcc peaks, confirming the IrO_2 crystallites being very small (Fig. 4l). We determined a coherence length of the rutile IrO_2 crystallite distribution of 1.75 nm by employing the Scherrer equation[52] alongside with peak width analysis of the integrated 211 SAED ring (Fig. 4l, AST-0). Assuming the IrO_2 particles to be single crystalline, this value corresponds to the mean crystallite diameter. This value is in good accordance with the layer thickness determined from HAADF-STEM images (1.4 ± 0.3 nm) underlining the assumption of the layer being oxidic.

If Ir clusters are oxidized, an influence on the activity is possible because active sites could be made available due to increased roughness.[50] This could contribute to the improved HFR-free potential for AST-0 and AST-freq in Fig. 2b. However, as mentioned before, an additional influence arises from activity and conductivity changes connected to oxidation state changes.[32,35,48]

Interestingly, a metallic contribution is not evident at EOT for AST-0 and -freq when analyzed with XPS (Fig. 3d). Additionally, the metallic contribution in the CVs (Fig. 3 and Fig. S4) vanishes the latest after 72 h of stress testing, hinting toward the fact that the surface contributing to electrochemical reactions is predominantly oxidic. XPS and CV are more surface sensitive than 4D-STEM and SAED, possibly explaining the observed differences. Notably, the thin oxide layer in the case of AST-amp and -CC (and additional amorphous phases) seems to shield the underlying metallic Ir to contribute to the reaction at EOT (Fig. 3c). Besides the methods used here, X-ray absorption spectroscopy (XAS) could complement our findings as bulk method to analyze the oxidation state of the CL.[18] Additionally, it shows potential as *operando* technique to observe changes in the oxidation state during operation.[53] However, beam damage effects have to be considered.

Metal ion migration and precipitation. The dissolution of active material, driven by oxidation state changes and redox cycling during periodic shutdowns, and under OER conditions, is anticipated.[5,22,35] In general, it was shown that the stability of Ir toward dissolution strongly depends on its oxidation state. Rutile Ir oxide showed the highest stability, followed by metallic Ir. The lowest stability was shown for hydrous Ir oxide.[3,6,34]

The migration of metal ions into the membrane is expected based on previous findings in the literature.[8] Redeposited particles in the membrane have been detected in all samples (Fig. S13 and S15). SAED of single particles within the membrane confirms that for all samples, the particles within the membrane have an fcc lattice and are thus assumed to be of metallic nature (Fig. 5g and Fig. S18k–t). Using a combination of a HAADF-STEM imaging series and a STEM-EDX point spectra series spanning the membrane from anode to cathode, we obtained statistics of the number of particles as well as their size distribution (Fig. 5f and Fig. S15) and elemental composition (Fig. 5e and Fig. S17).

An accumulation of particles in the close vicinity of the anode is visible in the raw data (Fig. 5a and Fig. S13f–j) and is evident from the particle count (Fig. 5f and Fig. S15) for all tests. We call it 'Ir cloud' because it consists of very small Ir clusters present in high density (see exemplary inset for AST-freq in Fig. 5a). The densest Ir cloud is visible for AST-amp (Fig. S13i).

Additionally, for AST-0 and -freq, another area with an increased number of larger particles close to the anode is observed. It is located roughly 2 μm from the Ir cloud, as can be seen from HAADF-STEM images (AST-0: Fig. S13b, AST-freq: Fig. 5b and Fig. S13c) and exhibits an increased mean particle diameter (AST-0: Fig. S15c, AST-freq: Fig. 5f and Fig. S15d). We further observe two areas with an increased number of particles starting from around 10 μm distance from both electrodes for all tests (Fig. 5f and Fig. S15). For AST-0 and -freq, these two peaks are also clearly visible in the mean particle radius distribution through the membrane. For AST-amp and -CC, the particle size distribution appears more homogeneous.

The elemental mapping (STEM-EDX point spectra) through the membrane (Fig. S17) reveals that particles contain not only Ir but also Pt. For AST-0 and -freq, the band 2 μm away from the anode exhibits ~50 at% of Ir and Pt, respectively (Fig. 5e and Fig. S17c, d). Hence, we denote this area spanning roughly 2–3 μm as 'Ir/Pt band' (Fig. 5b) analogous to a 'Pt band' observed for PEM fuel cells.[54] Starting from 10–15 μm from the anode, the particles consist predominantly of Pt (Fig. 5e and Fig. S17). For the conditioned sample, AST-amp and AST-CC (Fig. S17b, e and f), the particles starting from roughly 5 μm distance from the anode until the cathode consist mostly of Pt. Interestingly, close to the cathode, the Ir content rises again for the conditioned sample, AST-amp, and AST-CC. Ir within the cathode was only detected for AST-0. Pt within the anode CL was not detected *via* STEM-EDXS (Fig. S17b–f). Interestingly, XPS results show a signal of Pt for the stressed CL with AST-0, -freq and -amp (Fig. S6b and S7a). Note that XPS was measured on the anode CL side that was facing the PTL during testing. Hence, we assume that Pt is only present on the surface of the CL facing the PTL and most likely originates from the PTL coating.

We expect the position of particles within the membrane to be specific to the O_2 and H_2 partial pressure ratio determined by the crossover of the two gases. H_2 could act as a reductant for metal ions migrating through the membrane, leading to a precipitation of the metallic form.[54] It is further possible that ions deposit in the oxide form upon contact with O_2 and are

Open Access Article. Published on 10 lokakuuta 2025. Downloaded on 6.2.2026 15.34.04.
This article is licensed under a Creative Commons Attribution 3.0 Unported Licence.

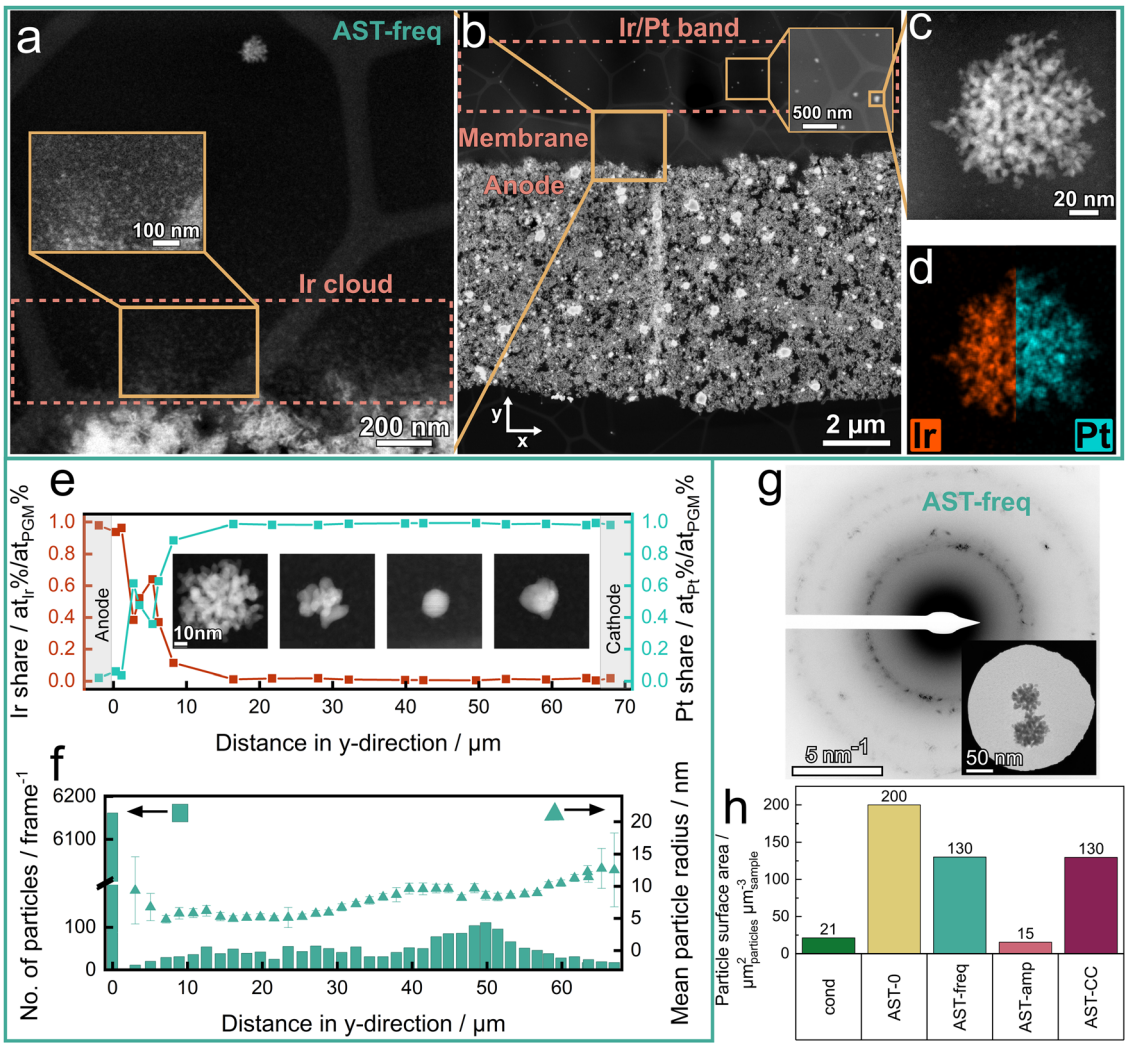

Fig. 5 (a)–(c) Exemplary HAADF-STEM images and (d) STEM-EDX spectrum images of a ~100 nm CCM slice after stress testing with AST-freq. Data for all stress tests can be found in Fig. S11 and S13. (e) Exemplary elemental composition from STEM-EDXS of particles detected within the membrane. Elemental compositions for all stress tests can be found in Fig. S17. (f) Exemplary particle statistics through the membrane from anode to cathode of EOT CCM sample from AST-freq. One frame is roughly 1.6 × 1.6 µm. Particle statistics for all stress tests can be found in Fig. S15. (g) SAED and selected area of particles detected within the membrane of AST-freq sample. (h) Normalized particle surface area derived from particle statistics (Fig. S15). To obtain the values, the lateral surface area of all analyzed particles is divided by the total analyzed sample volume.

afterwards reduced by H_2 crossing over. Further investigation is needed to determine if Ir and Pt are combined as an alloy, cluster, or as one element deposited onto the other.

The origin of the differences in metal ion precipitation between the different stress tests remains uncertain due to several aspects. The position-specific H_2 and O_2 concentrations are unknown and could be influenced by the testing protocol (occurrence and duration of low-potential periods). As observed from Fig. S15, reductive periods influence the mean size of the precipitated particles (AST-0 and -freq *vs.* AST-amp and -CC). It needs to be investigated if this is governed solely by the amount of dissolved metal, by how much the ion migration through the membrane is reduced during low-potential periods because of a lack of driving force, and how the crossover of gases is influenced. For AST-freq, a higher number of switching compared to AST-0 would be expected to result in more dissolution. However, the total time spent in low-potential periods or in operation is the same for both tests. Notably, within each hold period, ions have less time to migrate during AST-freq compared to AST-0. On the contrary, the driving force is continuously present for the other two protocols, AST-amp and -CC. However, less dissolution is expected due to the operation conditions (avoided redox transients).

In terms of crossover, insights for dynamic PEMWE operation remain incomplete. The exact gas concentrations within the anode, membrane, and cathode need further research.[55] For instance, it remains unclear to what extent the oxygen concentration at the cathode and in the membrane is reduced during OCV, as oxygen is not transported within the hydration shell of protons.[55] This could influence the recombination of O_2 and H_2 on the cathode, affecting the local hydrogen partial pressure and thus the hydrogen crossover. Moreover, it is

 This journal is © The Royal Society of Chemistry 2025

Open Access Article. Published on 10 lokakuuta 2025. Downloaded on 6.2.2026 15.34.04.
This article is licensed under a Creative Commons Attribution 3.0 Unported Licence.

unknown whether the hydrogen crossover might be increased because the diffusion from cathode to anode is not disrupted by an opposing transport of protons. Additionally, during idle periods, gas formation stops while active water flow removes gases from the anode and gases can diffuse out from the cathode. This leads to a time-dependent decrease in gas concentration on both electrodes. Consequently, the role of hydrogen as a reductant requires more investigation. The hydration of the membrane is another factor possibly impacting the solubility of gases in the membrane. It was shown that the water supply influences the Ir deposition in the membrane.[5]

Pt particles within the membrane can have different effects. Used as a recombination catalyst within the membrane, it was shown to increase the formation of radicals, leading to chemical degradation of the membrane.[56,57] Hence, the total particle surface area was chosen in this study as indicator for degradation on the long run. The total particle surface area from spherical approximation was normalized to the analyzed sample volume as depicted in Fig. 5h. It is obvious that for AST-0, the particles within the membrane exhibit the highest surface area. AST-freq and -CC are in a similar range. Interestingly, many small particles contribute to the surface area for AST-CC, whereas for AST-freq, fewer particles with a larger mean radius are present (Fig. S15). It is prominent that for all tests except AST-CC, the prevailing surface area is Pt (Fig. S17a). The Ir surface area for AST-CC is dominant due to many small particles in the first 10 μm into the membrane and the increase of Ir content toward the cathode. AST-amp shows a similar total particle surface area to the conditioned sample and is, therefore, possibly the mildest condition regarding enhancement of radical formation.

While the origin of dissolved Ir is unambiguous, the Pt within the membrane could have two possible sources: the PTL coating on the anode or the CL on the cathode. Whether dissolution is possible from the cathode CL was tested *via* a hydrogen pumping experiment. The goal was to observe the potential change on the cathode during shutdown periods when H_2 is diffusing out and, hence, the cathode deviates from its reference state (details in SI). It can be seen in Fig. S19, that a positive potential at which dissolution would take place ($\sim$800 mV [58]) has not been reached (max. $\sim$28 mV measured). Literature on cathodic corrosion in acidic media is sparse. However, we think it is unlikely to occur since the negative potentials observed are in the single digit millivolt range, rendering the cathode as the source of dissolved Pt unlikely. On the anode, however, a Pt-dissolving regime is present for all tests.[58] In the literature, Pt within the membrane was reported when Pt-based recombination layers or Pt-coatings of PTL or flow field were employed.[12,59] Hence, we assume that the Pt originates most likely from the PTL coating. It was shown that Pt dissolution is higher for the cathodic scan, *i.e.* the reduction of (electro-)chemically formed Pt oxide, than for the anodic scan (formation of Pt oxide). This could explain the increased particle surface area in Fig. 5h for the tests, which drag the potential below 1 V (*i.e.*, AST-0 and AST-freq).[36,58] Thus, Pt-coating – intended initially as a protective layer – could unexpectedly contribute to radical-induced membrane degradation when operating in intermittent mode.

Ir dissolves at low potentials or during shutdown,[58] and hydrous Ir oxide possesses lower dissolution stability.[6] Both could contribute to the increased dissolution seen for AST-0 and -freq (Fig. S15b and c).[22] The increased particle surface area present within the membrane for AST-CC is presumably driven by Ir because it also dissolves at higher potentials and during OER (Fig. S17a). For AST-amp, the operation at the lower current density of 1 A cm^{-2} 50% of the time seems to reduce the dissolution rate. An influence from the loss of Ir as active catalyst material on the performance is not expected to be visible due to the high loadings used.

As shown in Fig. S16b, when the sample is highly stressed as for AST-freq, the number and size of particles within the Ir/Pt band also fluctuate in *x*-direction (along the electrode). We hypothesize that this depends on the under-pore or under-fiber location since the fluctuations are in the same length scale as the pore-fiber dimensions.[60] Ma *et al.*[61,62] showed that the catalyst utilization is highest in contact with the PTL. Thus, we hypothesize that, at the contact areas with the PTL, either a higher gas concentration leads to increased particle precipitation or metal dissolution is enhanced.[46] Since the total mass of particles is similar along the *x*-direction (Fig. S16, right axis), an increased precipitation of particles is more likely instead of more dissolution. This emphasizes the need for an optimized CL|PTL interface design, such as the addition of a microporous layer on the PTL.[63,64] For the analysis of degradation this means that it is essential to analyze a representative sample area to capture spatial variations. To further strengthen the analysis, scale-bridging and multimodal techniques should be used and correlated (*e.g.*, XPS and CV in our study) to ensure reliability of observed phenomena. Additionally, using bulk measurement techniques to support the findings from the nanoanalysis (*e.g.*, X-ray diffraction to support SAED) could be valuable in the future. For an automized measurement and analysis, it should also be feasible to increase the sample area measured (several slices) and further increase the robustness of statistical trends.

A summary plot was constructed in Fig. 6 from selected analyses to directly compare the stress tests. It becomes evident that the four stress tests evoke different degradation mechanisms in a PEMWE cell configuration with Ir metal-based catalyst and a Pt-coated PTL. AST-freq shows the largest changes for ohmic resistances (ΔHFR). However, due to the initial performance improvement, the performance degradation is lower than observed for a CCM stressed with AST-amp and AST-CC (ΔE). AST-0 exhibits the highest particle loss, which can get detrimental in the context of membrane degradation and when employing low loadings. It is currently unknown which of the protocols would be suited as established AST since operation strategies from commercial operators are not published. However, this study enables extensive insights into the mechanisms depending on the operation. Together with a reference study on a CCM exposed to long-term (>3000 h) dynamic operation (*e.g.*, derived from electricity price), the

Open Access Article. Published on 10 lokakuuta 2025. Downloaded on 6.2.2026 15.34.04.
This article is licensed under a Creative Commons Attribution 3.0 Unported Licence.

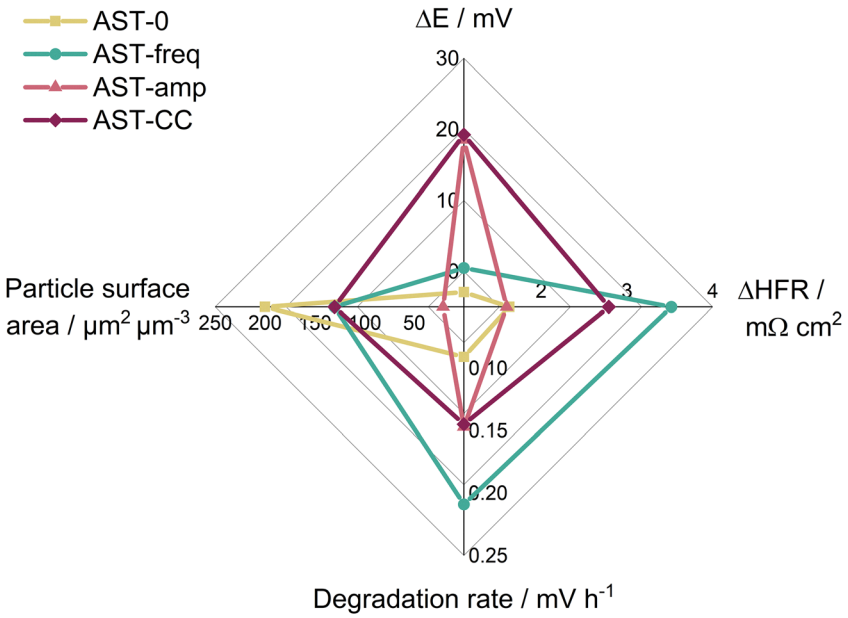

Fig. 6 Spider plot to visualize performance losses (ΔE and ΔHFR) and possible long-term degradation (degradation rate and particle surface area in the membrane) with the four stress tests. Note that for all parameters, a high value means more degradation or worse performance. The degradation rates shown are from the linear trend analysis.

obtained insights can be used to develop an operation- and catalyst-specific AST. In order to achieve a sensible comparison, the same components and materials need to be used, and regular characterization intervals are necessary.

Mitigation strategies for the increased risk of radical formation due to Pt particles within the membrane may include the incorporation of radical scavengers into the membrane.[57] Additionally, the hydrogen crossover should be minimized by operational approaches such as the rapid release of H_2 from the cathode during shutdown events, or membrane development, such as incorporating hydrogen-blocking interlayers.[65] In terms of oxidation state, a fully oxidized Ir surface is presumably favorable regarding long-term stability.

Conclusion

In summary, this study examines the degradation mechanisms emerging from four different accelerated stress protocols by applying correlative electrochemical analysis and *ex situ* techniques. We show that degradation originates from multiple interconnected mechanisms, which highly depend on the operation mode. One key finding is the dissolution of Pt from the anode-PTL coating. This can disrupt the critical interface between PTL and CL and lead to Pt deposition within the membrane, thereby increasing the risk of radical formation and chemical membrane degradation. Although Pt-coatings on Ti-based PTLs are commonly employed to prevent passivation and reduce contact resistance, their potential contribution to the degradation in PEMWE systems remains largely overlooked. These findings underline the importance of evaluating not only the CL but also assessing the long-term stability of components such as the PTL and their coatings. Any effective mitigation strategy must take these factors into account.

Additionally, changes in the oxidation state of the anode catalyst contribute to degradation by affecting catalytic activity and electronic conductivity. Interestingly, dynamic operation through redox potentials (AST-0 and -freq) results in a higher degree of rutile Ir oxide, which we assign to the repeated dissolution of the anhydrous oxide layer covering Ir metal. Notably, the cell performance in these two stress tests exhibits a distinct trend, where an initial performance improvement is followed by degradation. In contrast, when redox potentials are avoided, the performance degrades from the beginning of the test. Iridium dissolution is also evident for all stress protocols and is expected to become increasingly detrimental for the cell performance when reducing the catalyst loadings.

While polarization curves, electrochemical impedance spectroscopy, and cyclic voltammetry are established characterization tools for PEMWE, we demonstrated a powerful workflow employing complementary *ex situ* methods for quantifying structural and chemical changes and how they correlate with performance losses. In particular, we show the suitability of 4D-STEM, applied here for the first time for the spatially resolved identification of different phases within the CL. Nevertheless, current approaches to resolve ionomer degradation within the CL remain largely limited due to beam damage introduced by electron- or X-ray probes and necessitate further development.

Looking ahead, similar investigations must be conducted with iridium oxide-based catalysts, such as rutile IrO_2 or sub-stoichiometric IrO_x, to enable the development of a catalyst-type specific, sensible AST protocol. While the activity of oxidized Ir is lower than that of metallic Ir, its significantly higher stability could justify a trade-off in favor of enhanced

 This journal is © The Royal Society of Chemistry 2025

Open Access Article. Published on 10 lokakuuta 2025. Downloaded on 6.2.2026 15.34.04.
This article is licensed under a Creative Commons Attribution 3.0 Unported Licence.

long-term durability. To fully determine which protocol is best suited for accelerated materials development, a validation study is essential to compare the induced degradation mechanisms from the different stress protocols with real, long-term operation under an electricity-price load profile.

Materials and methods

Stress testing

Four different stress protocols have been designed based on energy price fluctuations.[27] The protocols are depicted in Fig. S1 and summarized in Fig. 1a. The base case (AST-0) consists of a square-wave protocol cycling between 2 A cm^{-2} and forced "OCV" (controlled to 27 mV) holding each step for 6 min. This protocol is compared to three variations: AST-freq, where the cycling frequency is increased 6-fold, AST-amp, where a shutdown is avoided and AST-CC, where cycling is avoided entirely.

Each testing protocol is applied four times for 24 h after conditioning of the cells with pristine CCMs with intermittent electrochemical characterization every 24 h. Additionally, beginning-of-test (BOT) and end-of-test (EOT) characterizations were conducted. For *ex situ* characterization, various techniques were applied to disassembled CCMs (XPS) as well as to 100 nm-thick slices of the CCMs from the four different test protocols and a reference CCM, which was in the PEMWE cell only for conditioning.

Electrochemical characterization

Electrode and catalyst-coated membrane (CCM) fabrication. CCMs were manufactured *via* the decal transfer technique where 5 cm^2-sized electrodes coated onto a PTFE substrate are united with a ~51 μm thick Nafion™ NR212 membrane (Chemours) by a hot-pressing step at 155 °C and 2.5 MPa. The loadings of the electrodes were determined by weighing the decals before and after hot pressing.

The catalyst inks were prepared from a mixture of the respective catalyst powder with suitable solvents and Nafion™ D2021 ionomer dispersion (Chemours). For the anode, an unsupported Ir black catalyst powder (≥98 wt% Ir, Umicore) was mixed with DI water, 1-propanol (>99.9%, Sigma-Aldrich), and the ionomer dispersion with a water to solvent ratio of 7.8 wt%, an ionomer to catalyst ratio of 12.17 wt% and a catalyst content of 0.46 g_{cat} ml_{ink}^{-1}.

For the cathode, platinum supported on carbon catalyst powder (40 wt% Pt/C, TEC10V40E, Tanaka Precious Metals) was mixed with DI water, 1-propanol, and the ionomer dispersion with a water to solvent ratio of 6.5 wt%, an ionomer to catalyst ratio of 28 wt% and a catalyst content of 0.05 g_{cat} ml_{ink}^{-1}.

The inks were homogenized for 24 h using a roller mixer (BTR5-12V, Ratek) with zirconium beads (5 mm diameter, Fritsch™ GmbH) at 180 rpm and 60 rpm for anode and cathode ink, respectively. The inks were used to coat electrodes onto 50 μm-thick PTFE substrate (High-tech-flon) using the Mayer rod technique (rods from ERICHSEN GmbH & Co. KG). The loading adjustment was achieved by using rods with different wire sizes (40 μm for anode and 100 μm for cathode electrodes). The electrode sheets were dried for 2 h at 70 °C (furnace ED56, BINDER) before being cut into 5 cm^2 electrodes and hot pressed with the membrane. CCMs with an anode loading of 1.65 ± 0.09 mg_{Ir} cm^{-2} and cathode loading of 0.15 ± 0.06 mg_{Pt} cm^{-2} were used in all tests.

Single-cell tests in PEMWE setup. All cell tests were performed on a commercial test bench (600 Electrolyzer Test System, Scribner LLC) equipped with a potentiostat with a current booster (BioLogic VSP-300). An in-house designed cell fixture adapted from previous reports[39] with a 5 cm^2 active area was used.

The respective CCM was assembled with a platinum-coated Ti-fiber PTL (2GDL10-0.25 with 0.2 μm Pt-coating from NV Bekaert SA) on the anode and a gas diffusion layer (GDL) with a microporous layer (MPL) consisting of carbon (H24C5 Freudenberg & Co. KG) on the cathode. Gasket thicknesses were chosen so that a compression of the carbon GDL of 22.1 ± 0.6% was achieved. For AST-CC a compression of only 17.1% was reached due to an abnormally thin PTL.

The anode was flushed with 100 mL min^{-1} DI water, which was additionally purged with nitrogen for 10 min prior to testing to remove any dissolved CO_2 from the tank's refill. The anode feed was heated to 80 °C, the cathode was kept dry, and only the venting line behind the cell was purged with nitrogen for safety reasons. The cell was heated to 80 °C with cartridge heaters placed into both endplates and regulated by a thermocouple placed into the cathodic flow field plate. Temperatures were kept constant throughout the whole testing time. When the cell temperature and anode feed reached 80 °C, the temperature was held for 30 min before starting the electrochemical testing.

Each test began with checking for electrical short *via* three potential steps at 1.1 V, 1.2 V, and 1.3 V. Subsequently, cyclic voltammetry (CV) was recorded with electrochemically produced H_2 (current hold at 1 A cm^{-2} for 5 min). Before starting the CV, the cell was held at 0.3 V for 30 s to reduce the produced oxygen from the anode. Four subsequent CVs are recorded between 0.1 and 1.45 V with a scan rate of 50 mV s^{-1}. For conditioning, the current was stepped up to 1 A cm^{-2} with 10 mA s^{-1} and held for 30 min. Another set of CVs was measured afterward with the same settings as before. For the following electrochemical impedance spectroscopy (EIS) measurement, H_2 was again produced electrochemically (produced oxygen could escape during a 30 s hold at 1.3 V). The EIS was performed potentiostatically in non-faradaic conditions (*i.e.*, at 1.25 V)[46] from 200 kHz to 1 Hz.

In the following, three subsequent polarization curves were recorded. The polarization curves were measured between 0.005 and 4 A cm^{-2}, holding each current density step for 5 min to ensure steady-state conditions and averaging the last 15 s for analysis. Galvanostatic EIS was performed from 200 kHz to 100 mHz at each point of the polarization curve after the respective current density hold. The perturbation of each AC current was chosen ≤10% of the AC current but not smaller than 20 mA so that a good signal-to-noise ratio was

Open Access Article. Published on 10 lokakuuta 2025. Downloaded on 6.2.2026 15.34.04.
This article is licensed under a Creative Commons Attribution 3.0 Unported Licence.

achieved, and a linear system response was ensured. Since the first two polarization curves were considered part of conditioning, an overlap of the last two curves was checked, and only the last polarization curve was taken for analysis. The beginning-of-test (BOT) characterization was repeated three times to ensure reproducibility.

Hydrogen pumping. A H_2-pumping experiment was done with a symmetric CCM comprising CLs with Pt/C (as described above) on both sides and a ~51 μm thick Nafion™ NR212 membrane. This CCM was sandwiched between two GDLs with MPL (Freudenberg, H24C5). In order to judge the overpotential the cathode experiences during the fast AST-0 and AST-freq protocols, H_2 pumping was executed as explained in detail in the SI with Fig. S19. The experiment was done on a test bench with an active hydrogen supply (Scribner 850e). The cell was conditioned with humidified H_2 on the counter electrode (CE; electrode for H_2 oxidation reaction) and synthetic air on the working electrode (WE; electrode for H_2 evolution reaction) for 10 h.[66] Prior to the experiment, the WE was flushed with N_2 (0.45 L min^{-1}) for 15 min to remove oxygen while the CE remained unchanged. The CE was supplied with humidified H_2 (0.2 L min^{-1}) during the experiment, and the WE was kept without flow, *i.e.* just as for the PEMWE measurements. The measurement was performed by galvanostatically drawing current from the WE according to AST-0 and AST-freq test protocols, subsequently repeating each for 1 h and recording the potential evolution.

Data evaluation from cell tests. High-frequency resistance (HFR) values were extracted from the galvanostatic electrochemical impedance measurements at each current density by fitting a frequency interval of 30–0.4 kHz with an equivalent circuit model comprising an inductance, a resistor, and a transmission line model in series.[67,68]

Electrode sheet resistance (ESR) values were extracted from potentiostatic EIS measurements at 1.25 V (non-faradaic region) by fitting a frequency interval of 200–0.02 kHz with an equivalent circuit model comprising an inductance, a resistor, and a blocking-type transmission line model in series.[46,67] Adjusted R^2 (R_{adj}^2) was used as a quality indicator for the fit. Fitting was performed using an in-house developed Python routine based on NumPy,[69] SciPy,[70] pandas,[71,72] matplotlib,[73] and impedance.py.[74]

HFR-free polarization curves were derived by subtracting the product of HFR and current density from the polarization curve. Tafel slopes were extracted from the HFR-free potential by a linear fit in a current density range of 5 to 50 mA cm^{-2} when plotted with a logarithmic current density axis.

Ex situ characterization

Powder conductivity. The powder conductivity was measured in a 3D-printed setup as described in detail in our group's earlier study.[75] The measurement is based on a four-electrode setup, and a Shimadzu EZ-SX testing machine ensures constant compression of the catalyst powder.

X-ray photoelectron spectroscopy (XPS). XPS was performed on the anode CL of all stress tests and selected PTLs. XPS measurements were performed using a Quantera II (Physical Electronics, Chanhassen), equipped with a monochromatic Al $K\alpha_1$-X-ray source (1486.6 eV), which was operated at 15 kV and 25 W. Automatic charge neutralization was used during all measurements and the spectra were measured over a circular area with a diameter of 100 μm. Besides recording narrow spectra at C 1s, O 1s, Pt 4f, and Ir 4f core levels, survey spectra were measured. The pass energy was set to 55 eV and the step size to 0.1 eV, except for the survey spectra, where a 0.2 eV step size was used. Analysis of the spectra was performed using the software CasaXPS.[76]

Scanning electron microscopy. For the cross-section imaging, 0.8 cm long pieces of the tested CCMs were sandwiched between two carbon GDLs and a 3D-printed holder, that was fixed with two screws. The sandwich was then embedded into epoxy resin (Buehler) and dried for 24 h in room temperature. Afterwards, the surface was ground and polished (Struers, LaboForce-100) to create a flat surface.

A Tescan Vega3 is used for secondary electron imaging at an acceleration voltage of 20 kV.

Preparation of ultramicrotomy slices. All following techniques have been performed on thin slices (~100 nm) of the CCM cross sections cut with an ultramicrotome. For this, a cut out (~2 mm × 5 mm) of the CCMs from the four stress tests (AST-0, -freq, -amp, -CC) and the conditioned sample was embedded in epoxy resin (electron microscopy science) and cured for 48 h at 60 °C (Binder oven ED56). Slices of ~100 nm were cut with an ultramicrotome (PowerTome PTPCZ, RMC Boeckler) and placed onto a TEM grid (Lacey carbon on copper, Micro to Nano BV).

Transmission electron microscopy. High-angle annular dark field scanning transmission electron microscopy (HAADF-STEM) was carried out using a Talos F200i (Thermo Fisher Scientific) featuring a Schottky-type field emission gun (X-FEG) operated at an acceleration voltage of 200 kV, a probe current of roughly 70 pA and a convergence angle of 10.5 mrad. STEM energy dispersive X-ray spectroscopy (STEM-EDXS) was performed with two attached Bruker XFlash 6|100 detectors in an energy range of up to 20 keV. Bright-field transmission electron microscopy (BF-TEM) and selected area electron diffraction (SAED) has been performed with the same tool and acceleration voltage employing selected area apertures of 200 μm, 40 μm, and 10 μm, respectively.

TEM analysis – SAED. SAED patterns were radially integrated and distortion corrected *via* a Python-based algorithm introduced in our previous work.[52] In short, the routine comprises automated center-finding, distortion correction up to 4th order, and radial profile integration. Reference spectra were retrieved from Inorganic Crystal Structure Database and q was calculated *via* the Bragg equation. Crystallographic data with collection number ICDS#659854 and ICDS#84577 for iridium and iridium oxide was used, respectively.

Procedure – point spectra for elemental distribution in CCM via EDXS. EDX point spectra were recorded by placing the STEM

 This journal is © The Royal Society of Chemistry 2025

Open Access Article. Published on 10 lokakuuta 2025. Downloaded on 6.2.2026 15.34.04.
This article is licensed under a Creative Commons Attribution 3.0 Unported Licence.

probe onto particles within the membrane and acquiring the signal for 60 s (trade-off between beam damage and signal-to-noise ratio). The spectra were recorded from anode to cathode in ~2-μm steps or larger when no changes were detected.

TEM analysis – elemental distribution analysis. Elemental analysis was done by using peak fitting routines of STEM-EDXS measurement implemented in Velox version 3.12. The respective contents are calculated normalized to the total measured content of Pt and Ir.

An explanatory figure for the procedure of elemental distribution can be found in Fig. S20.

Procedure – x- and y-scans. For *x*- and *y*-scans to obtain representative particle statistics images were recorded at medium magnification from adjacent regions parallel and perpendicular (*x*- or *y*-scan) to the membrane plane. The images had a resolution of 4k-by-4k pixels with an interpixel distance of ~0.4 nm (beam size at FWHM: 0.68 nm (ref. 77)) to avoid sub-sampling and to resolve particle sizes below 2 nm.

TEM analysis – x- and y-scan statistics. To investigate the particle statistics along a through-plane axis through the membrane from anode to cathode (*y*-scan) and for validation along the anode (*x*-scan), the raw intensity and original metadata were extracted from the microscope files using HyperSpy.[78] Image analysis was performed in FIJI.[79] To prepare for thresholding, a median filter with a 4-pixel radius was applied, followed by a Top Hat filter with a 25-pixel radius, while each image contains 4096 by 4096 pixels. Image areas covered by the metal TEM grid or the electrodes were cut out manually before thresholding. Note that cut-out areas are excluded from any subsequent analysis. Threshold calculation was performed with a triangle or Yen algorithm or by manually setting an intensity value, depending on the image quality. Next, the 'Analyze Particles' function in FIJI was used to extract isolated particles while excluding partially captured "edge" particles. Subsequent statistics were performed using an in-house Python routine harnessing pandas.[72] Here, the measured projected areas of the particles are converted into an equivalent radius by assuming a circle covering an equivalent area. Particles with an equivalent radius of up to 2 pixels were discarded as noise.

The total surface area of particles within the membrane was calculated directly from all detected particles of the *y*-scan analysis.

The surface area for platinum and iridium in Fig. S17a was calculated based on two areas where the averaging was performed. The first area spans from the anode until 10 μm into the membrane. The second area is the rest of the membrane area until the cathode. The electrodes are intentionally excluded for calculation. Averaging was done within these areas for particle size and elemental composition. The elemental composition was used together with the obtained count of particles from *y*-scan statistics to calculate the number of particles consisting of Ir or Pt. Finally, the number of particles and mean particle radius were used to determine the surface area.

The surface area is always normalized to the sample area analyzed from the *y*-scan statistics to compare between the tests.

An explanatory figure for the procedure can be found in Fig. S20.

Determination of area coverage from HAADF-STEM images. The area coverage was determined on the full electrode thickness along a distance of at least 50 μm. At least three measurement areas were averaged, and the value is given as mean value ± standard deviation.

Determination of oxide thickness from HAADF-STEM. The measurement of oxide thickness was performed with ImageJ.[80] The mean value ± standard deviation from at least seven measurement points is given.

4D-STEM. Nano-beam 4D-STEM experiments were carried out on a Thermo Fisher Scientific Spectra 200 TEM instrument equipped with a cold field emission gun and a probe Cs-corrector. The 4D-STEM datasets were acquired using a fast hybrid pixel detector (Dectris ARINA). Acquisition parameters are: a probe current of ~130 pA, a (nominal) convergence semi-angle of 0.47 mrad, a (nominal) camera length of 125 mm, a scanning step 2.13 nm pixel^{-1}, a dwell time of 100 μs (*i.e.*, 10 kHz), a scanning size of 512 × 512 pixels. The datasets are analyzed using the open-source package py4DSTEM (ver. 0.14.18).[81,82] In the phase matching, fcc Ir was manually defined with lattice parameter a = 3.86 Å, and the rutile phase was loaded from the .cif file with ICSD #56009.

In detail, the diffraction patterns at each probed positions are matched against a simulated library of all possible diffraction patterns of the given fcc and rutile phases. As a result, the highest matching score marks the phase at the probed position. Overlapping diffraction pattern sets (co-existing diffraction pattern from different phase/orientation is allowed) are enabled in the analysis. The Jupyter notebooks used for the analysis (with all used hyper-parameters) are provided in the SI and the raw data will be made available on Zenodo.

Author contributions

Selina Finger: conceptualization, data curation, formal analysis, investigation, methodology, project administration, validation, visualization, writing – original draft preparation, writing – review & editing. Birk Fritsch: methodology, software, validation, supervision, writing – review & editing. Mingjian Wu: investigation, formal analysis, writing – review & editing. Leopold Lahn: investigation, formal analysis, writing – review & editing. Darius Hoffmeister: investigation, formal analysis, writing – review & editing. Johannes Will: supervision, methodology, writing – review & editing. Erdmann Spiecker: funding acquisition, supervision, writing – review & editing. Olga Kasian: supervision, writing – review & editing. Simon Thiele: funding acquisition, resources, supervision, writing – review & editing. Anna T.S. Freiberg: conceptualization, methodology, resources, supervision, writing – review & editing. Andreas Hutzler: conceptualization, methodology, verification, investigation, formal analysis, data curation, project administration, supervision, writing – review & editing.

Open Access Article. Published on 10 lokakuuta 2025. Downloaded on 6.2.2026 15.34.04.
This article is licensed under a Creative Commons Attribution 3.0 Unported Licence.

Conflicts of interest

There are no conflicts to declare.

Data availability

The data supporting the 4D-STEM measurement are openly available in Zenodo at **https://doi.org/10.5281/zenodo.15781678**. The data that support all other findings of this study are available from the corresponding author upon reasonable request.

The SI includes additional Fig. S1–S20. See DOI: **https://doi.org/10.1039/d5ee03712c**.

Acknowledgements

The authors gratefully acknowledge the financial support by the German Federal Ministry of Research, Technology and Space (BMFTR) for the project StacIE (FKZ: 03HY103H) within the H2Giga flagship project. The authors would like to thank Lukas Löttert for valuable discussions, Khajidkhand Chuluunbandi for the H_2-pumping experiment, and Dennis Chalupczok for OCV measurements. Open access was organized *via* the German TIB Consortium.

References

1 C. R. Wang, J. M. Stansberry, R. Mukundan, H.-M. J. Chang, D. Kulkarni, A. M. Park, A. B. Plymill, N. M. Firas, C. P. Liu, J. T. Lang, J. K. Lee, N. E. Tolouei, Y. Morimoto, C. H. Wang, G. Zhu, J. Brouwer, P. Atanassov, C. B. Capuano, C. Mittelsteadt, X. Peng and I. V. Zenyuk, *Chem. Rev.*, 2025, **125**(3), 1257–1302.

2 Energy.gov, Technical Targets for Proton Exchange Membrane Electrolysis, available at: **https://www.energy.gov/eere/fuelcells/technical-targets-proton-exchange-membrane-electrolysis**, accessed 30 June 2025.

3 M. Möckl, M. F. Ernst, M. Kornherr, F. Allebrod, M. Bernt, J. Byrknes, C. Eickes, C. Gebauer, A. Moskovtseva and H. A. Gasteiger, *J. Electrochem. Soc.*, 2022, **169**, 64505.

4 H. Yu, L. Bonville, J. Jankovic and R. Maric, *Appl. Catal., B*, 2020, **260**, 118194.

5 S. M. Alia, K. S. Reeves, D. A. Cullen, H. Yu, A. J. Kropf, N. Kariuki, J. H. Park and D. J. Myers, *J. Electrochem. Soc.*, 2024, **171**, 44503.

6 S. M. Alia, K. S. Reeves, H. Yu, J. H. Park, N. N. Kariuki, A. J. Kropf, D. J. Myers and D. A. Cullen, *J. Electrochem. Soc.*, 2024, **171**, 24505.

7 U. Babic, M. Tarik, T. J. Schmidt and L. Gubler, *J. Power Sources*, 2020, **451**, 227778.

8 M. Milosevic, T. Böhm, A. Körner, M. Bierling, L. Winkelmann, K. Ehelebe, A. Hutzler, M. Suermann, S. Thiele and S. Cherevko, *ACS Energy Lett.*, 2023, **8**, 2682–2688.

9 S. H. Frensch, F. Fouda-Onana, G. Serre, D. Thoby, S. S. Araya and S. K. Kær, *Int. J. Hydrogen Energy*, 2019, **44**, 29889–29898.

10 N. Li, S. S. Araya and S. K. Kær, *Electrochim. Acta*, 2021, **370**, 137748.

11 J. Liu, H. Liu, Y. Yang, Y. Tao, L. Zhao, S. Li, X. Fang, Z. Lin, H. Wang, H. B. Tao and N. Zheng, *ACS Cent. Sci.*, 2024, **10**, 852–859.

12 A. Voronova, S. Kim, D. Kim, H.-Y. Park, J. H. Jang and B. Seo, *Energy Environ. Sci.*, 2023, **16**, 5170–5184.

13 S. Garbe, J. Futter, A. Agarwal, M. Tarik, A. A. Mularczyk, T. J. Schmidt and L. Gubler, *J. Electrochem. Soc.*, 2021, **168**, 44515.

14 C. Baik, J. Cho, J. Cha, Y. Cho, S. S. Jang and C. Pak, *J. Power Sources*, 2023, **575**, 233174.

15 E.-J. Kim, J. Shin, J. Bak, S. J. Lee, K. H. Kim, D. Song, J. Roh, Y. Lee, H. Kim, K.-S. Lee and E. Cho, *Appl. Catal., B*, 2021, **280**, 119433.

16 P. Holzapfel, M. Bühler, C. van Pham, F. Hegge, T. Böhm, D. McLaughlin, M. Breitwieser and S. Thiele, *Electrochem. Commun.*, 2020, **110**, 106640.

17 F. Hegge, F. Lombeck, E. Cruz Ortiz, L. Bohn, M. von Holst, M. Kroschel, J. Hübner, M. Breitwieser, P. Strasser and S. Vierrath, *ACS Appl. Energy Mater.*, 2020, **3**, 8276–8284.

18 S. M. Alia, K. S. Reeves, H. Yu, J. Park, N. Kariuki, A. J. Kropf, D. J. Myers and D. A. Cullen, *J. Electrochem. Soc.*, 2022, **169**, 54517.

19 X. Shi, X. Qiu, Z. Yuan, R. Zhang, K. Zhao, A. Tan, G. Xu, J. Song and J. Liu, *ACS Appl. Mater. Interfaces*, 2024, **16**, 66089–66098.

20 E. Kuhnert, K. Mayer, M. Heidinger, C. Rienessel, V. Hacker and M. Bodner, *Int. J. Hydrogen Energy*, 2024, **55**, 683–695.

21 A. Voronova, H.-J. Kim, J. H. Jang, H.-Y. Park and B. Seo, *Int. J. Energy Res.*, 2022, **46**, 11867–11878.

22 A. Weiß, A. Siebel, M. Bernt, T.-H. Shen, V. Tileli and H. A. Gasteiger, *J. Electrochem. Soc.*, 2019, **166**, F487–F497.

23 C. Spöri, C. Brand, M. Kroschel and P. Strasser, *J. Electrochem. Soc.*, 2021, **168**, 34508.

24 A. J. McLeod, L. V. Bühre, B. Bensmann, O. E. Herrera and W. Mérida, *J. Power Sources*, 2024, **589**, 233750.

25 S. F. Zaccarine, M. Shviro, J. N. Weker, M. J. Dzara, J. Foster, M. Carmo and S. Pylypenko, *J. Electrochem. Soc.*, 2022, **169**, 64502.

26 J. Gerhardt-Mörsdorf, F. Peterssen, P. Burfeind, M. Benecke, B. Bensmann, R. Hanke-Rauschenbach and C. Minke, *Adv. Energy Sustainable Res.*, 2024, **5**, 2300135.

27 Prof. Dr. Bruno Burger, Börsenstrompreise|Energy-Charts, available at: **https://www.energy-charts.info/charts/price_spot_market/chart.htm?c=DE&legendItems=2x1i0&week=07**, accessed 30 June 2025.

28 S. M. Alia, S. Stariha and R. L. Borup, *J. Electrochem. Soc.*, 2019, **166**, F1164–F1172.

29 P. J. Rheinländer and J. Durst, *J. Electrochem. Soc.*, 2021, **168**, 24511.

30 S. M. Alia, B. Rasimick, C. Ngo, K. C. Neyerlin, S. S. Kocha, S. Pylypenko, H. Xu and B. S. Pivovar, *J. Electrochem. Soc.*, 2016, **163**, F3105–F3112.

31 S. Cherevko, S. Geiger, O. Kasian, N. Kulyk, J.-P. Grote, A. Savan, B. R. Shrestha, S. Merzlikin, B. Breitbach, A. Ludwig and K. J. Mayrhofer, *Catal. Today*, 2016, **262**, 170–180.

 This journal is © The Royal Society of Chemistry 2025

Open Access Article. Published on 10 lokakuuta 2025. Downloaded on 6.2.2026 15.34.04. This article is licensed under a Creative Commons Attribution 3.0 Unported Licence.

32 S. Cherevko, S. Geiger, O. Kasian, A. Mingers and K. J. Mayrhofer, *J. Electroanal. Chem.*, 2016, **774**, 102–110.
33 S. Gottesfeld and S. Srinivasan, *J. Electroanal. Chem. Interfacial Electrochem.*, 1978, **86**, 89–104.
34 M. Zlatar, X. Xie, C. Franke, T. Hrbek, Z. Krtouš, T. Li, I. Khalakhan and S. Cherevko, *EES Catal.*, 2025, **3**, 521–534.
35 S. Cherevko, S. Geiger, O. Kasian, A. Mingers and K. J. Mayrhofer, *J. Electroanal. Chem.*, 2016, **773**, 69–78.
36 S. Cherevko, N. Kulyk and K. J. Mayrhofer, *Nano Energy*, 2016, **29**, 275–298.
37 S. M. Alia, M.-A. Ha, G. C. Anderson, C. Ngo, S. Pylypenko and R. E. Larsen, *J. Electrochem. Soc.*, 2019, **166**, F1243–F1252.
38 A. Hartig-Weiss, M. Miller, H. Beyer, A. Schmitt, A. Siebel, A. T. S. Freiberg, H. A. Gasteiger and H. A. El-Sayed, *ACS Appl. Nano Mater.*, 2020, **3**, 2185–2196.
39 M. Bernt and H. A. Gasteiger, *J. Electrochem. Soc.*, 2016, **163**, F3179–F3189.
40 V. Pfeifer, T. E. Jones, J. J. Velasco Vélez, C. Massué, R. Arrigo, D. Teschner, F. Girgsdies, M. Scherzer, M. T. Greiner, J. Allan, M. Hashagen, G. Weinberg, S. Piccinin, M. Hävecker, A. Knop-Gericke and R. Schlögl, *Surf. Interface Anal.*, 2016, **48**, 261–273.
41 *Handbook of X-ray photoelectron spectroscopy. A reference book of standard spectra for identification and interpretation of XPS data*, ed. J. F. Moulder and J. Chastain, PerkinElmer Physical Electronics Div, Eden Prairie, Minn. 1992.
42 C. Roiron, C. Wang, I. V. Zenyuk and P. Atanassov, *J. Phys. Chem. Lett.*, 2024, **15**, 11217–11223.
43 P. G. Pickup and V. I. Birss, *J. Electroanal. Chem. Interfacial Electrochem.*, 1987, **220**, 83–100.
44 S. Cherevko, T. Reier, A. R. Zeradjanin, Z. Pawolek, P. Strasser and K. J. Mayrhofer, *Electrochem. Commun.*, 2014, **48**, 81–85.
45 K. Kuribayashi and S. Kitamura, *Thin Solid Films*, 2001, **400**, 160–164.
46 E. Padgett, G. Bender, A. Haug, K. Lewinski, F. Sun, H. Yu, D. A. Cullen, A. J. Steinbach and S. M. Alia, *J. Electrochem. Soc.*, 2023, **170**, 84512.
47 Y.-S. Li, D. Menga, H. A. Gasteiger and B. Suthar, *J. Electrochem. Soc.*, 2023, **170**, 94503.
48 M. Bernt, C. Schramm, J. Schröter, C. Gebauer, J. Byrknes, C. Eickes and H. A. Gasteiger, *J. Electrochem. Soc.*, 2021, **168**, 84513.
49 D. Böhm, M. Beetz, C. Gebauer, M. Bernt, J. Schröter, M. Kornherr, F. Zoller, T. Bein and D. Fattakhova-Rohlfing, *Appl. Mater. Today*, 2021, **24**, 101134.
50 M. van der Merwe, Y. Lee, R. E. Wibowo, T. Kokumai, A. Efimenko, M. D. Arce, C. E. Jimenez, B. Howchen, R. Suarez Anzorena, I. Lucentini, C. Escudero, G. Schuck, Z. Kochovski, M. Favaro, D. E. Starr, K. Reuter, C. Scheurer, M. Bär and R. Garcia-Diez, *Energy Environ. Sci.*, 2025, **18**, 1214–1231.
51 T. Seip, N. Shaigan, M. Dinu, K. Fatih and A. Bazylak, *J. Power Sources*, 2023, **559**, 232654.
52 B. Fritsch, M. Wu, A. Hutzler, D. Zhou, R. Spruit, L. Vogl, J. Will, H. Hugo Pérez Garza, M. März, M. P. M. Jank and E. Spiecker, *Ultramicroscopy*, 2022, **235**, 113494.
53 L. Almeida De Campos, P. Ciocci, J. Schröder and T. L. Sheppard, *ChemCatChem*, 2025, e00530.
54 J. Zhang, B. A. Litteer, W. Gu, H. Liu and H. A. Gasteiger, *J. Electrochem. Soc.*, 2007, **154**, B1006.
55 A. T. S. Freiberg and S. Thiele, *J. Electrochem. Soc.*, 2025, **172**, 34506.
56 M. Zatoń, J. Rozière and D. J. Jones, *Sustainable Energy Fuels*, 2017, **1**, 409–438.
57 Z. Zhang, Z. Han, A. Testino and L. Gubler, *J. Electrochem. Soc.*, 2022, **169**, 104501.
58 S. Cherevko, A. R. Zeradjanin, A. A. Topalov, N. Kulyk, I. Katsounaros and K. J. J. Mayrhofer, *ChemCatChem*, 2014, **6**, 2219–2223.
59 Z. Zeng, R. Ouimet, L. Bonville, A. Niedzwiecki, C. Capuano, K. Ayers, A. P. Soleymani, J. Jankovic, H. Yu, G. Mirshekari, R. Maric and S. Bliznakov, *J. Electrochem. Soc.*, 2022, **169**, 54536.
60 M. Bierling, D. McLaughlin, B. Mayerhöfer and S. Thiele, *Adv. Energy Mater.*, 2023, **13**, 2203636.
61 T.-C. Ma, A. Hutzler, B. Bensmann, R. Hanke-Rauschenbach and S. Thiele, *J. Electrochem. Soc.*, 2024, **171**, 44504.
62 T.-C. Ma, A. Hutzler, R. Hanke-Rauschenbach and S. Thiele, *Electrochem. Commun.*, 2025, **178**, 107965.
63 T. Schuler, C. C. Weber, J. A. Wrubel, L. Gubler, B. Pivovar, F. N. Büchi and G. Bender, *Adv. Energy Mater.*, 2024, **14**, 2302786.
64 K. Bobzin, S. Finger, L. Zhao, H. Heinemann, E. Olesch, K. Radermacher, S. Pechmann, D. Possart, S. H. Christiansen, D. Hoffmeister, B. Fritsch, S. Thiele and A. Hutzler, *Adv. Eng. Mater.*, 2025, **27**, 2402462.
65 M. Komma, A. T. S. Freiberg, D. Abbas, F. Arslan, M. Milosevic, S. Cherevko, S. Thiele and T. Böhm, *ACS Appl. Mater. Interfaces*, 2024, **16**, 23220–23232.
66 G. S. Harzer, PhD thesis, Technische Universität München, 2018.
67 J. Landesfeind, J. Hattendorff, A. Ehrl, W. A. Wall and H. A. Gasteiger, *J. Electrochem. Soc.*, 2016, **163**, A1373–A1387.
68 R. Makharia, M. F. Mathias and D. R. Baker, *J. Electrochem. Soc.*, 2005, **152**, A970.
69 C. R. Harris, K. J. Millman, S. J. van der Walt, R. Gommers, P. Virtanen, D. Cournapeau, E. Wieser, J. Taylor, S. Berg, N. J. Smith, R. Kern, M. Picus, S. Hoyer, M. H. van Kerkwijk, M. Brett, A. Haldane, J. F. Del Río, M. Wiebe, P. Peterson, P. Gérard-Marchant, K. Sheppard, T. Reddy, W. Weckesser, H. Abbasi, C. Gohlke and T. E. Oliphant, *Nature*, 2020, **585**, 357–362.
70 P. Virtanen, R. Gommers, T. E. Oliphant, M. Haberland, T. Reddy, D. Cournapeau, E. Burovski, P. Peterson, W. Weckesser, J. Bright, S. J. van der Walt, M. Brett, J. Wilson, K. J. Millman, N. Mayorov, A. R. J. Nelson, E. Jones, R. Kern, E. Larson, C. J. Carey, İ. Polat, Y. Feng, E. W. Moore, J. VanderPlas, D. Laxalde, J. Perktold, R. Cimrman, I. Henriksen, E. A. Quintero, C. R. Harris, A. M. Archibald, A. H. Ribeiro, F. Pedregosa and P. van Mulbregt, *Nat. Methods*, 2020, **17**, 261–272.
71 The pandas development team, pandas-dev/pandas: Pandas, DOI: **10.5281/zenodo.3509134**.

Open Access Article. Published on 10 lokakuuta 2025. Downloaded on 6.2.2026 15.34.04.
This article is licensed under a Creative Commons Attribution 3.0 Unported Licence.

72 W. McKinney, Proc. of the 9th Python in Science Conference, 2010, pp. 56–61.
73 J. D. Hunter, *Comput. Sci. Eng.*, 2007, **9**, 90–95.
74 M. Murbach, B. Gerwe, N. Dawson-Elli and L. Tsui, *J. Open Source Software*, 2020, **5**, 2349.
75 D. Hoffmeister, S. Finger, L. Fiedler, T.-C. Ma, A. Körner, M. Zlatar, B. Fritsch, K. W. Bodnar, S. Carl, A. Götz, B. A. Zubiri, J. Will, E. Spiecker, S. Cherevko, A. T. S. Freiberg, K. J. J. Mayrhofer, S. Thiele, A. Hutzler and C. van Pham, *Adv. Sci.*, 2024, **11**, e2402991.
76 N. Fairley, V. Fernandez, M. Richard-Plouet, C. Guillot-Deudon, J. Walton, E. Smith, D. Flahaut, M. Greiner, M. Biesinger, S. Tougaard, D. Morgan and J. Baltrusaitis, *Appl. Surf. Sci. Adv.*, 2021, **5**, 100112.
77 A. Körner, B. Fritsch, A. L. Morales, P. Malgaretti and A. Hutzler, *Nano Today*, 2025, **61**, 102575.
78 F. De La Peña, E. Prestat, V. T. Fauske, P. Burdet, J. Lähnemann, P. Jokubauskas, T. Furnival, M. Nord, T. Ostasevicius, K. E. MacArthur, D. N. V. Johnstone, A. Eljarrat, J. Caron, C. Francis, T. Nemoto, T. Poon, S. Mazzucco, N. Tappy, N. Cautaerts, S. Somnath, T. Slater, M. Walls and F. Winkler, *hyperspy/hyperspy:v2.2.0*, 2024, available at: **https://zenodo.org/records/14057415**.
79 J. Schindelin, I. Arganda-Carreras, E. Frise, V. Kaynig, M. Longair, T. Pietzsch, S. Preibisch, C. Rueden, S. Saalfeld, B. Schmid, J.-Y. Tinevez, D. J. White, V. Hartenstein, K. Eliceiri, P. Tomancak and A. Cardona, *Nat. Methods*, 2012, **9**, 676–682.
80 C. A. Schneider, W. S. Rasband and K. W. Eliceiri, *Nat. Methods*, 2012, **9**, 671–675.
81 C. Ophus, S. E. Zeltmann, A. Bruefach, A. Rakowski, B. H. Savitzky, A. M. Minor and M. C. Scott, *Microsc. Microanal.*, 2022, 1–14.
82 B. H. Savitzky, S. E. Zeltmann, L. A. Hughes, H. G. Brown, S. Zhao, P. M. Pelz, T. C. Pekin, E. S. Barnard, J. Donohue, L. Rangel DaCosta, E. Kennedy, Y. Xie, M. T. Janish, M. M. Schneider, P. Herring, C. Gopal, A. Anapolsky, R. Dhall, K. C. Bustillo, P. Ercius, M. C. Scott, J. Ciston, A. M. Minor and C. Ophus, *Microsc. Microanal.*, 2021, **27**, 712–743.

 This journal is © The Royal Society of Chemistry 2025